

1 **Observations of stratocumulus clouds and their effect on the eastern Pacific surface**
2 **heat budget along 20°S**

3

4 Simon P. de Szoeke

5 Sandra Yuter

6 David Mechem

7 Chris W. Fairall

8 Casey Burleyson

9 Paquita Zuidema

10

11 Submitted to *J. Climate*

12 October 2011

13

14 **Abstract**

15 Widespread stratocumulus clouds were observed on 9 transects from 7 research cruises to
16 the southeastern tropical Pacific Ocean along 20°S, 75°-85°W in October-November
17 2001-2008. The nine transects sample a unique combination of synoptic and interannual
18 variability affecting the clouds; their ensemble diagnoses longitude-vertical sections of
19 the atmosphere, diurnal cycles of cloud properties and drizzle statistics, and the effect of
20 stratocumulus clouds on surface radiation. Cloud fraction was 0.88 and most 10-minute
21 overhead cloud fraction observations were overcast. Clouds cleared in the afternoon (15 h
22 local) to a minimum of fraction of 0.7. Precipitation radar found strong drizzle with
23 reflectivity above 40 dBZ.

24

25 Cloud base heights rise with longitude from 1.0 km at 75° to 1.2 km at 85°W in the mean,
26 but the slope varies from cruise to cruise. Cloud base-lifting condensation level (CB-
27 LCL) displacement, a measure of decoupling, increases westward. At night CB-LCL is 0-
28 200 m, and increases 400 m from dawn to 16 h local time, before collapsing in the
29 evening.

30

31 Despite zonal gradients in boundary layer and cloud vertical structure, surface radiation
32 and cloud forcing are relatively uniform in longitude. Clouds reduce solar radiation by -
33 160 W m^{-2} and radiate 70 W m^{-2} more downward longwave radiation than clear skies.
34 Coupled model intercomparison project (CMIP3) simulations of the climate of the 20th
35 century show $40 \pm 20 \text{ W m}^{-2}$ too little net cloud radiative cooling at the surface. Simulated
36 clouds have correct radiative forcing when present, but models have ~50% too few
37 clouds.

38

39 **1. Introduction**

40 Accurate simulation of tropical southeastern Pacific Ocean sea surface temperature (SST)
41 is challenging for coupled general circulation models (GCMs; Mechoso et al. 1995,
42 Davey et al. 2002, de Szoeke and Xie 2008). Warm errors of 2°C in SST are found at
43 20°S, 75°W in most of the Coupled Model Intercomparison Project phase 3 (CMIP3)
44 models assessed by de Szoeke et al. (2010). Atmospheric subsidence over cool SST and
45 high surface pressure provides a stable cap to the marine boundary layer, reducing the
46 cloud-top entrainment rate and increasing stratiform clouds (Klein and Hartmann 1993).

47 The high-albedo clouds shade the ocean surface from strong tropical solar radiation, thus
48 cooling it. This positive feedback between shallow clouds and SST helps to maintain
49 more low stratus and stratocumulus clouds and cooler SST in the southern hemisphere
50 than the northern hemisphere eastern tropical Pacific. The north-south symmetry is
51 broken by trade-wind driven upwelling at the northwest-southeast slanted American coast
52 (reviewed by Xie 2004). The clouds and their feedbacks are difficult to simulate
53 accurately because critical turbulence and precipitation processes are parameterized in the
54 atmospheric models. Testing models and improving parameterizations thus call for
55 detailed observations of stratus cloud processes.

56

57 Figure 1 shows the location of cool tropical SST (shaded) and the stratocumulus cloud
58 deck (cloud fraction, contoured) for climatological average October-November AMSR
59 SST (Risien and Chelton 2008) and MODIS cloud fraction (Platnick et al. 2003). De
60 Szoeke et al. (2010) shows Coupled Model Intercomparison Project (CMIP3) 20th
61 century GCM simulations with $20\text{-}30\text{ W m}^{-2}$ excess net surface radiative warming
62 compared to satellite and in situ observations. The downwelling excess solar and reduced
63 longwave radiation is consistent with too little simulated cloud or simulated clouds with
64 weaker radiative properties than observed. Here we explore sensitivity of observed
65 surface downwelling radiation to cloud fraction, atmospheric temperature and water
66 vapor profiles, cloud boundaries, and liquid water path.

67

68 Cronin et al. (2006) and Fairall et al. (2008) measure the effect of marine clouds on the
69 tropical Eastern Pacific heat budget using observations from TAO buoys along 95° and

70 110°W, the Woods Hole Oceanographic Institution (WHOI) Stratus buoy at 20°S, 85°W,
71 and ship observations from the buoy-tending cruises. We perform a similar radiative
72 analysis for research cruises to the stratocumulus region along 20°S between 85° and
73 75°W. Kollias et al. (2004) documents cloud and marine boundary layer vertical structure
74 using rawinsondes, cloud remote sensing, and aerosol sampling on a research cruise in
75 the stratocumulus region in 2003. We combine observations in the 20°S eastern Pacific
76 stratocumulus region from research cruises in 2001 and 2003-2008. All but one of the
77 research cruises were in October-November.

78

79 Section 2 introduces the ship-based observations of clouds, drizzle, related surface
80 meteorology, radiative fluxes, and atmospheric rawinsondes. Section 3 presents the mean
81 vertical-longitude section of cloud properties. Section 4 presents the diurnal cycle of
82 clouds and section 5 assesses the effect of clouds on the surface radiation budget. Section
83 6 provides an example of how these cloud observations can be used to assess clouds in 15
84 GCMs used for climate projection. Section 7 summarizes the conclusions.

85

86 **2. Ship-based Observations**

87 In situ surface meteorology, cloud remote sensing, and rawinsonde observations were
88 collected aboard NOAA research cruises to the southeastern tropical Pacific Ocean in
89 2001, 2003, 2004, 2005, 2006, and 2007, culminating in 2008 with the VOCALS
90 (VAMOS Ocean Cloud Atmosphere Land Study, Wood et al. 2010). De Szoeker et al.
91 (2010) compiled and documented these data in the Tropical Eastern Pacific Synthesis

92 data set, and used surface flux observations from the synthesis data set to evaluate
93 CMIP3 models. Here we summarize cloud observations from the synthesis data set.
94
95 Ships yearly serviced the Woods Hole Oceanographic Institution (WHOI) Stratus Ocean
96 Reference Station at 20°S, 85°W (Colbo and Weller 2007) and the Chilean tsunami buoy
97 at 20°S, 75°W. NOAA PSD scientists made observations on research cruises to the
98 southeastern tropical Pacific Ocean along 20°S, 75°-85°W in 7 years (2001, 2003, 2004,
99 2006-2008). A total of eight 20°S sections (3 in 2008) by the instrumented ships are
100 included in the NOAA synthesis data set. Tracks of the ships for the nine sections are
101 plotted in Fig. 1. Dates of reaching destinations at 75° and 85°W are listed for each track
102 in the key below.

103

104 For the VOCALS Regional Experiment (REx) in 2008 the NOAA ship *Ronald H. Brown*
105 made 3 longitudinal along 20°S sections in 2 legs. In the first leg it made an eastward
106 section between servicing the WHOI Stratus Station and the Chilean tsunami buoy. On
107 the second leg the *Brown* made an east-west-east round trip from Arica, Chile to survey
108 ocean eddies. All 20°S transects, except for the ocean survey in the second leg of
109 VOCALS REx, were completed in under 3 days.

110

111 *Atmospheric soundings*

112 In all, 487 rawinsondes profiled temperature, humidity, and vector winds of the
113 troposphere in the vicinity of 20°S. Every 4 or 6 hours a rawinsonde was released from
114 the fantail of the ship during the cruises. The frequency of rawinsondes allows sampling

115 of atmospheric diurnal cycles, day-to-day variability, and gradients in longitude along
116 20°S. In 2005 soundings are available only west of 82°W. Maximum spacing between the
117 rawinsonde launches is 130 km, based on a ship's maximum speed of 12 nautical miles
118 per hour (6.2 m s^{-1}), but usually the distance between rawinsondes is much less.

119

120 *Surface meteorology and fluxes*

121 Surface air temperature and relative humidity are measured from a mast 17.5 m above sea
122 level at the bow of the ship. SST of the upper 5 cm of seawater is measured with a “sea
123 snake” floating thermistor. The surface lifting condensation level (LCL) and its
124 temperature is computed by adjusting the observed humidity and temperature to 500 m
125 according to similarity theory, then adiabatically lifting air with those properties until it is
126 saturated.

127

128 Downwelling solar and longwave radiative fluxes were measured by a pyranometer and a
129 pyrgeometer mounted on an upper deck of the ship. Upwelling radiative fluxes are
130 modeled from the albedo of the sea surface (0.05) and Planck blackbody radiation from
131 the SST, assuming the sea surface emissivity is 0.97. Clear-sky solar fluxes were
132 computed from the model of Iqbal (1988) using the solar zenith angle and integrated
133 water vapor in the atmosphere. Clear-sky longwave radiation is computed from the Hare
134 (2005) 2-parameter model based on latitude and surface specific humidity. A 3-parameter
135 clear-sky model also using integrated water vapor has -2 W m^{-2} weaker downwelling
136 longwave radiation. Since the 3-parameter model is within sampling variability of the 2-
137 parameter model, we use the simpler 2-parameter model.

138

139 *Cloud remote sensing*

140 Passive and active remote sensing instruments measured properties of clouds over the
141 ship. Vertically pointing narrow-band microwave radiometers measured sky brightness
142 temperature T_B at 24 and 31 GHz (~1.5 and 1 cm), from which liquid water path (LWP)
143 and water vapor path (WVP) are calculated (Zuidema et al. 2005). A Vaisala pulsed lidar
144 ceilometer measured optical backscatter in the atmosphere, and retrieved the occurrence
145 of clouds and cloud base height of up to three clouds along its vertically pointing beam.
146 Cloud fraction is computed from 10-minute averages of cloud occurrence from the
147 ceilometer.

148

149 Cloud top height was computed by a variety of in situ and remote sensing methods. A
150 strong inversion was always present in the vicinity of 20°S, and was coincident with
151 cloud top when clouds were present. The rawinsondes detect inversion base height from
152 the coincident sharp rise in temperature and drop in humidity. The inversion base is
153 identified as the minimum temperature below the strongest gradient of temperature in the
154 lower 3 km of the troposphere. In 2001 and 2004-07 a NOAA 915-MHz wind profiler
155 retrieved boundary layer inversion height more frequently from Bragg scattering at the
156 gradient in atmospheric index of refraction at the inversion. In 2001, 2003, and 2008
157 cloud radar detected cloud top height as the highest range gate containing cloud
158 reflectivity above the radar noise threshold. Different measures of cloud top height were
159 found to agree when they coincided, though not all were available at any one time. Cloud

160 top height from cloud radar is found to be coincident within 10 m of inversion base
161 height from radiosondes for stratocumulus clouds over the southeastern tropical Pacific.
162
163 The 10-minute 15th, 50th, and 85th percentiles of cloud base height sampled every 20 s
164 by pulsed lidar ceilometer are recorded in the synthesis data set. These percentiles are
165 less influenced by outliers than the mean. The ceilometer sometimes returns cloud base
166 height from clouds above or below the stratocumulus cloud layer. Solar noise is a
167 problem for ceilometer cloud detection for high ranges when the sun was near zenith. For
168 stratocumulus cloud base height, we use the 85th percentile cloud base height to
169 minimize the contribution of boundary layer shallow cumulus below the stratocumulus,
170 and exclude cloud bases detected above the stratocumulus cloud top.

171

172 *Aerosol concentrations*

173 Aerosol number concentration (diameter $D > 0.1 \times 10^{-6}$ m) was measured by Texas A&M
174 University (TAMU, Tomlinson et al. 2007) in 2003 and 2004. In 2005, 2006, and 2007
175 the number is computed as the sum of aerosols counted by a Particle Measurement
176 Systems Lasair-II. Differences between sensitivity of the two instrument platforms may
177 affect the absolute accuracy, yet each detects relative changes in the size-resolved drop
178 concentrations. In 2008 the Pacific Marine Environmental Laboratory (PMEL) measured
179 aerosols aboard the ship (Covert, pers. communication). Three particle diameter bins
180 were chosen to be uniform across both platforms: 0.1-0.3, 0.3-1.0, and >1.0 μm .
181 Accumulation mode aerosols ($D > 0.1$ μm) have critical supersaturation less than 0.17%,
182 while coarse mode aerosols ($D > 1$ μm) have critical supersaturation less than 0.01%.

183 Aitken mode aerosol ($D < 0.1 \times 10^{-6}$ m) concentrations were measured by TAMU and
184 PMEL.

185

186 *Radar observations*

187 Doppler precipitation radar (C-band, 5 cm wavelength) made range-height and azimuthal
188 scans at different elevation angles every 3-10 minutes in 2001, 2004, and 2006-08. The
189 C-band radar provides reflectivity and radial velocity within a 60 km radius of the ship.
190 In 2001, 2003, and 2004 the vertically pointing NOAA millimeter-wavelength cloud
191 radar (MMCR, 8.6 mm) measured clouds and precipitation from the ship (Kollias 2004,
192 Comstock et al. 2004, Comstock et al. 2007). In VOCALS 2008 NOAA deployed a new
193 motion-stabilized W-band (3 mm) Doppler cloud radar sensitive enough to detect clouds
194 and capable of measuring precipitation drop and cloudy air vertical velocities (Moran et
195 al. 2011). In VOCALS 2008 the NOAA W-band measured high-resolution cloud and
196 precipitation reflectivity and vertical velocities, while the C-band simultaneously sampled
197 the larger surrounding area and mesoscale organization of precipitating structures (Yuter
198 et al. pers. communication).

199

200 **3. The Cloud-capped Boundary Layer Section Along 20°S**

201 *a. Thermodynamics and wind*

202 Measurements from rawinsondes released from research cruises along 20°S are presented
203 as longitude-height sections for 2001, 2003, 2004, 2006-2008 in Fig. 2. Multiple
204 soundings from when the ship was on station have been eliminated for clarity of
205 presentation, leaving 157 soundings shown in Fig. 2. Potential temperature and specific

206 humidity gradients show a well-mixed boundary layer 1.0-1.8 km deep. The mean
207 boundary layer potential temperature over all 8 sections is 290 ± 1 K. The boundary layer
208 is capped by a strong (10 K) inversion, over which the free troposphere has a 6.2 K km^{-1}
209 stable potential temperature gradient. Slightly stable stratification within the upper
210 boundary layer is occasionally observed, e.g. in 2008 leg 1 (Fig. 2k) east of 78°W and leg
211 2.2 (Fig. 2o) west of 81°W . The moist-adiabatic lapse rate of boundary layer
212 stratocumulus clouds causes this conditionally stable potential temperature stratification.
213 Conditionally stable potential temperature gradients are nearly ubiquitous in the top 100-
214 400 m of the boundary layer, where clouds are almost always observed. Stable layers are
215 also sometimes observed below the cloud layer, presumably evidence of decoupling of
216 warmer potential temperature air in the upper boundary layer from the cooler surface
217 mixed layer.

218

219 Fig. 2 shows boundary layer potential temperature is quite uniform in longitude,
220 increasing approximately 2 K from 75° to 85°W . This increase corresponds to the 2°C
221 SST gradient (Fig. 1). Temperature varies among the 20°S transects. Warmer temperature
222 and higher specific humidity are observed in 2003 and 2004. These transects occurred
223 later in the year, in late November and early December, when SST is seasonally higher.
224 Free tropospheric temperature is also higher and more stably stratified in December 2004,
225 which may contribute to capping the boundary layer to only about 1 km height. Such
226 cases must be interpreted with caution however, since synoptic variability influences the
227 soundings, but is not resolved by the cruise data. The three transects in 2008 show
228 boundary layer potential temperature progressively increasing about 1 K over the month

229 from October 27 to November 28. Assuming the seasonal cycle repeats each year we
230 attribute some differences in the sampled atmospheric profiles to their time in the
231 seasonal cycle. Though SST and the atmospheric structure also vary interannually, the 8
232 transects sample at best 2 El Niño/Southern Oscillation (ENSO) periods, so we cannot
233 estimate interannual variability with statistical certainty with this data set.

234

235 Water vapor specific humidity distinctly marks the inversion between the moist boundary
236 layer and the dry free troposphere (Fig. 2 right column). Specific humidity is 7-10 g kg⁻¹
237 and decreases with height in the boundary layer. This specific humidity gradient is found
238 in individual soundings. The specific humidity gradient below the cloud, where potential
239 temperature is constant, must be achieved by dry adiabatic processes. The constant
240 gradient of specific humidity suggests a layer mixing between two end members: the
241 moist surface layer and the drier cloud layer. Specific humidity in the free troposphere is
242 usually below 1 g kg⁻¹ and always distinctly drier than the MABL. Combined with the
243 increase of temperature at the inversion, the drier air results in a dramatic drop of relative
244 humidity, from saturation in the MABL cloud to less than 5% relative humidity in the
245 lower free troposphere (Fig. 3a)

246

247 The height of the boundary layer increases westward in 2001, 2006, 2007, and 2008 leg
248 2, but little or no westward tilt is evident in 2003, 2004, or 2008 leg 1. During VOCALS
249 REx, aircraft traversed 20°S from Arica, Chile to 80°W in and above the boundary layer
250 15 times from 2008 October 15 to November 13 (Bretherton et al. 2010). The slope of the
251 boundary layer depth also varied among these flights. Seeing this variability on

252 interannual to daily timescales, we conclude that considerable synoptic variability affects
253 the boundary layer clouds, which the yearly research cruises sample but do not resolve.

254

255 The shaded frequency-altitude diagrams in Fig. 3 show the vertical structure of the
256 temperature and humidity distribution of all 487 soundings within 2° of 20°S , $75\text{-}85^\circ\text{W}$.
257 The median (solid) and mean (dashed) profiles differ from the mode (dots) of the
258 distribution. This is especially true in the vicinity of the inversion, where the rise and fall
259 of inversion height results in sampling properties distributed bimodally between
260 boundary layer and free-tropospheric air, yet rarely a mixture of the two air masses. The
261 altitude-resolved distribution of thermodynamic variables indicates the sharpness of the
262 inversion. While the mean smoothes the inversion over 500 m, the modes of the
263 temperature and humidity distributions jump from boundary layer to free tropospheric
264 properties over only tens of meters, with few intermediate values.

265

266 Figure 3a shows relative humidity (RH) is about 70% at the surface, increasing linearly
267 with height in the boundary layer. The mode of the soundings is saturated (RH=100%) in
268 the top 500 m of the boundary layer, indicating clouds are usually present. The median
269 and mean RH are less than 100%, skewed toward unusual soundings that are unsaturated
270 at a given height. Thermodynamic profiles in Fig. 3 are bimodally distributed between
271 the clear free-troposphere air and boundary layer clouds near the inversion. Arithmetic
272 means over nonlinear transitions, such as between saturated and unsaturated air, are a
273 poor representation of clouds. Statistics of clouds will be explored further in subsection
274 3b.

275

276 The mean profile of wind along 20°S has vertically uniform 7 m s⁻¹ southeasterlies (u and
277 v components each 5 m s⁻¹) throughout the boundary layer, except for a 100-m thick layer
278 at the surface with what appears to be a logarithmic velocity profile (Fig. 4). The mean
279 profile has uniform northwesterly shear above the inversion, reaching westerlies of $u = 22$
280 m s⁻¹ and northerlies of $v = -11$ m s⁻¹ at 13 km altitude in the subtropical jet. Winds
281 change gradually across the inversion compared to the thermodynamic variables. The
282 standard deviation of zonal wind is 3 m s⁻¹ in the boundary layer and 4 m s⁻¹ above the
283 inversion. The standard deviation of meridional wind is 2 m s⁻¹ in the boundary layer and
284 3 m s⁻¹ above the inversion.

285

286 Thermodynamic atmospheric soundings are remarkably constant over the 7 years of
287 research cruises to 20°S. We idealized a sounding to 14 significant levels based on the
288 487 soundings along 20°S (Table 1).

289

290 *b. Clouds*

291 The size and frequency of clouds critically affect the surface heat budget through their
292 effect on surface radiation. Figure 5a shows the longitude-height section of mean MABL
293 top, cloud base, and lifting condensation level (LCL) in 2.5° longitude bins from 75 to
294 85°W along 20°S. The filled gray boxes show the mean top and bottom of the cloud,
295 while the unfilled boxes show standard deviation of the mean. The standard deviation of
296 the mean is computed over all 10-minute samples in the selected location, but the
297 variability is dominated by transect-to-transect variations. Each of the 9 transects is an

298 independent sample of synoptic, seasonal, and interannual variability. Cloud thickness
299 averages 230 m across the transect. The MABL top height and cloud base height increase
300 westward on average, with little change in mean cloud thickness. The range of cloud
301 heights includes cases in which the cloud height did not increase with longitude (cf. Fig.
302 2). Cloud heights were at the low end of the distribution in 2004 December—late in the
303 seasonal cycle—but did not differ much compared to cloud heights observed other years
304 in October and November. Excluding 2004 raises mean cloud heights by about 20 m, a
305 difference within the range of variability among October-November transects.

306

307 The LCL is the height at which we expect an undilute parcel from 500 m (transformed
308 with similarity theory from measurements at 15.5 m) to reach saturation with respect to
309 water vapor if it cools adiabatically as it is lifted. This is the lowest level that a cloud is
310 likely to form. While cloud base heights increase westward, LCL remains approximately
311 level, decreasing westward by only a statistically insignificant amount (Fig. 5a). The
312 least-squares regression of distance between cloud base and the LCL rises 30 m per 100
313 km of longitude. Figure 2 shows cloud base from the ceilometer (blue dots) is sometimes
314 within 100 m of the LCL (red dots), e.g. 2007 between 80-77°W. More often, cloud base
315 is several hundred meters above the LCL. The model of Bretherton and Wyant (1997)
316 predicts entrainment of warm dry air from above the boundary layer dilutes saturated
317 cloud air and evaporates clouds from their base, creating a warm decoupled sub cloud
318 layer. Displacement of the cloud base from the LCL is consistent with the decreasing
319 humidity gradient between the surface mixed layer and cloud base.

320

321 Cloud fraction (gray circles Fig. 5b) shows a weak decreasing trend westward from 92%
322 coverage at 75°W to 84% at 85°W. The middle 3 longitudes of cloud fraction and LWP
323 are averaged together at 80°W. Liquid water path (LWP) increases westward by 40%
324 over 10° longitude, despite decreasing cloud fraction (Fig. 5b). LWP in Fig. 5 is averaged
325 regardless of whether a cloud is present. Average LWP conditionally sampled in the
326 cloud would be slightly greater. Average liquid water content (LWC), increases 1 g m^{-3}
327 km^{-1} per km of cloud thickness. For an undilute cloud condensing water above its
328 saturation vapor pressure at the moist adiabatic lapse rate LWC would increase by 1.7 g
329 m^{-3} per km of cloud thickness.

330

331 *c. Aerosol concentrations*

332 Coarse and accumulation mode aerosol concentration (diameter $> 0.1 \times 10^{-6} \text{ m}$) was
333 measured in 2003-2008 (TAMU, Tomlinson et al. 2007), by a Lasair-II optical particle
334 sampler in 2005-2007, and by researchers from University of Washington and Pacific
335 Marine Environmental Laboratory (UW/PMEL) in 2008 (Cover, pers. communication).
336 Aerosol concentration increases toward the coast in all the 20°S longitude cross-sections
337 (Fig. 6a). South America is a source of dust. Its volcanoes, cities, and industries,
338 including copper smelters, are a source of sulfur dioxide, an aerosol precursor gas. Mean
339 concentration and standard deviation west and east of 80°W are displayed either side of
340 the longitude series. There appear to be systematic differences between TAMU and the
341 Lasair-II aerosol concentrations sampled, with lower concentrations measured by the
342 Lasair-II. Histograms of the concentration at 85°W show a wide range of concentrations
343 in 25 cm^{-3} bins from 0 to 300 cm^{-3} from the TAMU observations, and a narrower range of

344 lower concentrations ($75\pm 25\text{ cm}^{-3}$) from the Lasair-II (Figs. 6b and c). The two
345 instruments sampled distinct air masses each year they were used, which may have had
346 different aerosol concentrations. From the distributions of the TAMU and Lasair-II
347 aerosol concentrations, there may be a bias between the two sensors. Nevertheless the
348 gradient of aerosol concentration toward the coast is unambiguous. Aerosol concentration
349 is $150\text{-}250\text{ cm}^{-3}$ at 75°W , and mostly less than 100 cm^{-3} and relatively uniform west of
350 82°W .

351

352 Hypotheses conceived prior to VOCALS assumed that marine air masses at 85°W were
353 pristine. In fact the coarse and accumulation mode aerosol concentration at 85°W is about
354 half the concentration at 75°W . Rather than pristine, the aerosol concentration at 85°W is
355 variable, with standard deviation comparable to that at 75°W .

356

357 Liquid water path (LWP) decreases toward the coast (Fig. 5) while aerosols increase.
358 Aerosol concentration decreases as they are removed by precipitation and diluted farther
359 over the open ocean. LWP increases westward due to thicker low clouds. By separating
360 LWP at 85°W , where most of the aerosol concentrations were measured, into different
361 aerosol concentration bins, we should be able to see any emergent relationship between
362 LWP and aerosol concentration. Compared to the anticorrelation of aerosol concentration
363 and LWP over longitude, there is no systematic relationship between LWP and aerosol
364 concentration at 85°W . Competing cloud-aerosol effects could lead to this lack of a
365 relationship. Higher aerosol number increases LWP through cloud lifetime effect
366 (Albrecht 1989), while high LWP clouds remove aerosols by precipitation.

367

368 *d. Remote sensing of clouds and rain*

369 Instruments of different wavelengths and scanning strategies are used to detect clouds
370 and precipitation. Sensitive lidar (905 nm) ceilometers and cloud radars (3-mm W-band
371 and 8.6-mm MMCR) have a range of order 10 km and detect clouds overhead pointing
372 vertically. The W-band cloud radar used a vertical resolution of 25 m. Larger
373 precipitation particles have higher reflectivity and can be detected with longer
374 wavelength radar (5 cm C-band) at farther ranges. Strong precipitation occupies a small
375 area compared to the widespread southeastern tropical Pacific stratocumulus clouds. With
376 low elevation angle scans the C-band radar samples these infrequent events over a 60 km
377 radius area.

378

379 Figure 7 shows the fraction of sky detected above the threshold on the horizontal axis, for
380 research cruise legs along 20°S. Reflectivities lower than the receiver noise have been
381 excluded from the fraction. More clouds are detected as the method becomes more
382 sensitive at lower thresholds.

383

384 The linear scale of Fig. 7a emphasizes sensitivity and total cloud amount detected by
385 each instrument. The ceilometer, W-band cloud radar, and C-band precipitation
386 simultaneously sensed clouds and precipitation in 2008 VOCALS leg 2. The ceilometer
387 uses optical backscatter ($\text{km}^{-1} \text{steradian}^{-1}$, top axis) while the radars used reflectivity
388 (dBZ) units. The ceilometer is the most sensitive, detecting cloud fraction of 0.94 above
389 the threshold of $0.05 \text{ km}^{-1} \text{ sr}^{-1}$. The W-band cloud radar detects cloud fraction of 0.8

390 above -32 dBZ, and the C-band radar detects 0.61 cloud fraction above -20 dBZ. The
391 MMCR from 2003 is more sensitive than the W-band used in 2008. Though different
392 clouds were observed in 2003 and 2008, the reflectivity distributions are similar between
393 the MMCR and the W-band cloud radar (Fig. 7b).

394

395 The true fraction probably resembles the maximum of the fraction measured by the
396 ceilometer, the W-band, and the C-band radars in Fig. 7b. Only the ceilometer reliably
397 detects clouds with reflectivity less than -30 dBZ. The cloud radars detect cloudy and
398 drizzling columns with reflectivity -30 to -10 dBZ. All three radars had adequate
399 sensitivity and sampling from -25 to 15 dBZ, and their probability densities match.

400

401 Radar receivers saturate at high reflectivity. At 500 m range the W-band cloud radar
402 saturates at 33 dBZ (Moran et al. 2011), yet the number columns the W-band radar
403 observes above even 20 dBZ is insignificant. We suspect the vertically pointing radars
404 see too little sky to sample rare strongly precipitating events.

405

406 The C-band radar scans over a larger area and samples infrequently occurring cases of
407 high reflectivity. C-band fraction has a wide shoulder with 0.3% of pixels with
408 reflectivity above 20 dBZ. This shoulder decays more slowly with reflectivity than the
409 probability density in the 0-10 dBZ range. More than 10^5 pixels (0.03% of the total) are
410 over 50 dBZ, which corresponds to roughly $N=10^4$ 1-mm raindrops per meter³ for a
411 typical lognormal drop size distribution. Such reflectivity is unexpectedly high for warm

412 clouds, and implies warm microphysical processes generate large precipitation drops in
413 southeastern tropical Pacific stratocumulus cloud region.

414

415 **4. Diurnal Cycle**

416 *Cloud layer*

417 Low cloud fraction c is estimated in 10-minute averages from the pulsed lidar ceilometer,
418 which points vertically with a narrow field-of-view. To focus on stratocumulus clouds,
419 only clouds below 2 km are counted in c . This excludes infrequent high clouds and noise
420 contamination at higher ranges. The laser ceilometer ranges cloud base reflectivity within
421 a narrow field of view (<1 degree) directly overhead. Averaging the overhead cloud
422 fraction time series over an arbitrarily long time should give a mean cloud fraction that
423 approaches the entire sky cloud fraction. We choose a sampling interval of 10 minutes to
424 obtain a representative overhead cloud fraction and resolve cloud variability. Clouds
425 being so widespread, 71% of 10-minute overhead cloud fractions were totally cloudy
426 ($c=1$), and only 6% were clear ($c=0$), leaving 23% partly cloudy scenes ($0 < c < 1$).

427

428 Ceilometer cloud fraction c for the 7 years is composited on the local hour of the day
429 (Fig. 8a triangles). Mean cloud fraction goes through a single cycle each day, with
430 maximum of 0.96 at 4 in the morning and partly clearing to a cusp-shaped minimum of
431 $c=0.68$ in the afternoon (15 local). Cloud fraction is greater than 0.8 apart from 6 hours of
432 partial clearing in the afternoon. Shading in Fig. 8a shows fraction of observations by
433 hour-of-day that are overcast ($c=1$, dark gray), partly cloudy ($0 < c < 1$, light gray), or clear

434 ($c=0$, white). Afternoon clearing occurs with a 36% decrease in the number of overcast
435 observations.

436

437 While cloud base remains relatively constant throughout the day, cloud top varies from
438 1.27 to 1.43 km (Fig. 8b). Cloud thickness is 340 m in the early morning (0-6 h local) and
439 230 m in the afternoon (12-18 h local, Fig. 8b). If entrainment were solely responsible for
440 the growth of cloud top at night we would expect entrainment of dry air would also thin
441 the cloud layer, evaporating its base. Thickening of the cloud layer when the cloud top is
442 growing indicates that variation in subsidence, and not entrainment alone, contributes to
443 the diurnal variation in cloud top height. Figure 8c shows liquid water path (LWP) mean
444 (circles) and hourly 15, 30, 50, 70, and 85th percentiles. The LWP distribution is
445 positively skewed, biasing the mean toward higher values. The daily cycle of LWP is in
446 phase with cloud thickness, but changes relatively more than cloud thickness.

447

448 The ratio of LWP to cloud thickness is the vertical average liquid water content (LWC, g
449 m^{-3}) of the cloud. Squares in Fig. 8c show vertically averaged LWC for all sky (black),
450 and normalized by cloud fraction for the in-cloud average LWC when a cloud is present
451 (gray). The diurnal cycle of average LWC mostly follows the cycle of LWP, but
452 increases faster around 18 h when LWP increases but clouds stay relatively thin until
453 later in the evening. In fact in-cloud vertical average LWC is lowest at in the early
454 afternoon (2-3 h). Average LWC should increase nearly linearly with cloud thickness.
455 From the moist adiabatic lapse rate ($6.5 K km^{-1}$) and change in saturation LWC with
456 temperature ($5.5 \times 10^{-4} g m^{-3} K^{-1}$), we estimate vertical average LWC should increase 1.7

457 g m^{-3} per kilometer of cloud thickness for an undilute moist saturated air parcel. The least
458 squares fit of average LWC to cloud thickness variations over the diurnal cycle explains
459 0.6 g m^{-3} LWC per kilometer of cloud height. The difference is likely the result of several
460 plausible factors: Cloud fraction or the vertical extent of clouds may be overestimated by
461 the remote sensing instruments, clouds are diluted with warm or dry air, and/or liquid
462 water is precipitating out of the cloud. Precipitation must evaporate or reach the surface
463 before it is no longer sensed as LWP by the microwave radiometer.

464

465 *Subcloud layer variability*

466 Measurements of clouds and surface air temperature and humidity, combined with
467 conservation of heat and humidity, give us a *thermodynamic* definition of cloud
468 decoupling from surface layer air. This is complementary to definitions of kinematic
469 decoupling, measured as a minimum in vertical velocity variance or negative buoyancy
470 flux below cloud base.

471

472 The vertical structure of clouds and the sub-cloud boundary layer varies regularly over
473 the day. Surface lifting condensation level (LCL) is computed by adjusting the observed
474 humidity and temperature to 500 m according to similarity theory, then adiabatically
475 lifting air with those properties until it is saturated. The frequency distribution of
476 displacement of the cloud base height observed by the ceilometer from the LCL is
477 composited for each local hour of the day in Fig. 9. The mode of cloud base–LCL
478 displacement (circles, Fig. 9a) along 20°S reaches a maximum of 375 m at 14-15 local
479 and is near zero at 23-6 local. Figure 9b-d isolates the diurnal cycle in 3 longitude ranges.

480

481 The e^{-1} correlation time scale of the raw cloud base-LCL (CB-LCL) time series is 15
482 hours. Much of this is due to the diurnal cycle. The correlation time scale of the
483 anomalies drops to 6 hours when mean diurnal and zonal variations are removed. Though
484 observations are correlated for several consecutive hours, observations each day are
485 independent of observations from other days.

486

487 Despite changes in its amplitude, the pattern of the diurnal cycle is largely the same at
488 different longitudes. At each longitude CB-LCL displacement is relatively low and
489 constant during the night hours, only beginning to increase after sunrise at 6 local. The
490 displacement increases gradually through the morning until the mid afternoon. In each
491 longitude range maximum CB-LCL displacements are seen in the mid-afternoon, with
492 width of the CB-LCL displacement also increased in the afternoon. The mode of CB-
493 LCL displacement drops sharply about an hour before sunset at 17 hours local. All the
494 cloud base height-LCL distributions are bimodal in the late afternoon. Most at 85°W
495 observations at 9-16 local show cloud base height 400-650 m above the LCL, about twice
496 the displacement at 75°W . Even at night, the mode CB-LCL displacement is 100-200 m
497 at 85°W , compared to near zero at 75°W .

498

499 Black lines in each panel of Fig. 9 show normalized frequency distributions of CB-LCL
500 displacement for longitude bins in Table 2. Consistent with the mean LCL and cloud base
501 height in Fig. 5, the peak of the CB-LCL distribution rises westward for the longitude
502 bins in Fig. 9. At 75°W (Fig. 9d) cloud base height is a median of 75 m above the LCL,

503 indicating subcloud mixed layers with minimal humidity gradient and nearly adiabatic
504 lapse rate. At 80°W cloud base height is a median of 150 m above the LCL, and at 85°W
505 median displacement is 240 m. Cloud base-LCL displacement is more broadly distributed
506 to higher values 85° than at 75°W.

507

508 Comparisons of cloud base height and LCL suggest three mechanisms of thermodynamic
509 decoupling. The first is a uniform *offset* of the cloud base distribution upward from the
510 LCL, demonstrated by the upward shift of the mode of the cloud base height-LCL
511 displacement from 75° to 85°W. As one moves westward, this mode of relatively well-
512 coupled clouds are slightly more decoupled from the surface layer. Second, the
513 distributions in Fig. 9 suggest the *width* of the distribution broadens so that CB-LCL
514 displacement is more variable. The increased width indicates some cloud base parcels
515 have been diluted by larger quantities of warmer, drier air. Dilution by warmer drier air is
516 episodic and affects different clouds by a randomly varying amount. The offset and width
517 of the cloud base height distribution are independent of the LCL. Third, perhaps there is
518 *height-dependent* decoupling, with CB-LCL displacement correlated to the height of the
519 LCL itself. Diurnal composites in Fig. 10 suggest height-dependent decoupling only in
520 the afternoon, the most decoupled phase of the diurnal cycle.

521

522 Figure 10 shows joint distributions of cloud base height and LCL for different longitudes
523 and phases of the diurnal cycle. Columns are sorted by longitude; rows by 6-hour time
524 bin (0-6, 6-12, 12-18, and 18-24 local). Early morning (0-6 local) at 75°W is the most
525 thermodynamically coupled with 500-1000 m cloud bases forming at the LCL (Fig. 10i).

526 Cloud bases are most displaced from the LCL at 85°W. Afternoons at 75° and 85°W
527 (Figs. 11c,k) seem to show height-dependent decoupling, with larger displacements for
528 higher LCL, but even for these cases the correlations of CB-LCL displacement to the
529 LCL is unconvincing. While height-dependent decoupling would increase the regression
530 slope, wider distribution of cloud base height weakens the regression. Though LCL is a
531 lower bound for cloud base height, regressions of cloud base height on CB-LCL are
532 weak.

533

534 Separation of cloud base from the LCL is somewhat coordinated with diurnal changes in
535 cloud fraction and LWP (Fig. 8). On the whole CB-LCL displacement is largest in the
536 afternoon while cloud fraction is lowest. Cloud fraction begins to increase in the late
537 afternoon (15-18 h), a couple of hours before the fall of CB-LCL displacement. This
538 could be an indication that the rapid recoupling of the cloud to the surface layer is driven
539 by buoyancy flux from cloud-top radiative cooling after the stabilizing effects of
540 shortwave radiation are reduced in the late afternoon.

541

542 *Diurnal-longitude structure of clouds and tropospheric waves*

543 Models (Garreaud and Muñoz 2005, Rahn and Garreaud 2010) and satellite observations
544 (O'Dell 2008, Zuidema and Painemal 2009, O'Neill et al. 2011) show a first-harmonic
545 diurnal cycle in liquid water path (LWP) and cloud top height at 20°S 85°W. A strong
546 semidiurnal cycle is found at 75°W. Ship measurements composited hourly by local solar
547 time provide the highest available temporal resolution of the diurnal cycle along 20°S.
548 These data confirm modeling and remote sensing observations of the diurnal and
549 semidiurnal oscillations of LWP and cloud top height. Figure 11a-f are contoured

550 Hovmöller diagrams of key boundary layer and cloud properties as a function of local
551 solar time vs. longitude between 75° and 85°W. Data are composited in the three
552 longitude bins of Table 2. Mean zonal gradients (Fig. 5) exist throughout the diurnal
553 cycle with less cloud, higher SST, higher humidity, higher cloud tops, and higher liquid
554 water to the west.

555

556 The diurnal and semidiurnal harmonics explain most of the variance of boundary layer
557 variables (Fig. 12). The first harmonic explains more than 70% of the variance of the
558 diurnal cycle of cloud fraction, SST, and specific humidity (Fig. 12a-c). The diurnal and
559 semidiurnal components of the cloud fraction explain about the same fraction of variance
560 as the cosine of solar zenith angle: 0.84 for diurnal and 0.15 for semidiurnal. At 85°W
561 SST has diurnal and semidiurnal components in about this proportion, perhaps because
562 cloud fraction is low enough for solar absorption to drive SST. Cloud fraction and SST
563 lag incoming solar radiation by about 6 hours.

564

565 The first diurnal harmonic explains more than 90% of the variance of the surface specific
566 humidity, but water vapor path (WVP) has a strong semidiurnal rather than diurnal cycle
567 at 75°W. Thus boundary layer cloud and water vapor do not integrate away high-
568 frequency specific humidity variability. Diurnal variations in water vapor also do not
569 follow saturation vapor pressure of the SST. The peak surface specific humidity lags the
570 peak mid-afternoon SST by about 2 hours (Fig. 11b-c), but the specific humidity
571 minimum occurs 2 hours before sunrise, leading SST. Water vapor path is correlated
572 more strongly to cloud top height than to surface specific humidity. Because of the strong

573 specific humidity interface at the inversion, water vapor path is modulated more by
574 boundary layer height than internal changes in the boundary layer specific humidity.

575

576 As previously found in models and satellite observations, cloud top height, LWP, and
577 WVP have significant semidiurnal cycles at 20°S 75°W. All are linked more strongly to
578 the extent of the boundary layer than to intrinsic properties within the boundary layer.

579 The semidiurnal component of the boundary layer height comes from an offshore
580 propagating “upsidence” wave in tropospheric velocity, predicted by models to originate
581 from diurnal heating over the Andes.

582

583 We test the ship data for evidence of propagation from 75° to 85°W with cyclic lag
584 correlation (Fig. 12g-i). LWP and cloud top height at both 75° and 85°W have significant
585 first-harmonic diurnal cycles in phase with the solar cycle, with no time lag between 75°
586 and 85°W. Only water vapor path (WVP) has a lag of ~10 hours between 85° and 75°W,
587 but the correlations between 75° and 85°W are weak because the semidiurnal cycle
588 dominates at 75°W and the diurnal cycle dominates at 85°W.

589

590 An explanation posited for the lack of semidiurnal cycle at 85°W is destructive
591 interference of the local solar cycle and the propagating upsidence wave. This
592 explanation requires the semidiurnal component of the wave at 85°W to be the same
593 magnitude and of opposite phase as the local semidiurnal cycle driven by solar heating.

594 Gravity wave speeds of 30 m s^{-1} would give a time delay of 10 hours between 75° and
595 85°W. This is longer than the 6 hours it takes for the semidiurnal wave to reverse phase

596 locally, inconsistent with the destructive interference hypothesis. We propose that either
597 spatial interference between waves generated over Peru and Chile, and/or dissipation of
598 the semidiurnal upsidence wave, could be responsible for the small semidiurnal cycle at
599 85°W.

600

601 **5. Surface Cloud Radiative Forcing**

602 Clouds influence the transmission of solar radiation. From downwelling solar radiation
603 measured by pyranometer S and modeled clear-sky solar radiation S_1 (Iqbal 1988) we
604 compute the full solar transmissivity ratio $t = S/S_0$. Figure 13 shows the transmissivity for
605 all conditions (black) and cloudy (blue), partly cloudy (gray), and clear (magenta)
606 conditions as a function of the time of day. Each point represents a 10-minute average
607 realization along 20°S, 75-85W. Observations near dawn and dusk are less reliable
608 because S_0 is small due to the low solar elevation. We find in practice t can be only be
609 measured during daylight when the denominator S_0 is above 25 W m^{-2} . Solar
610 transmissivity is important only during significant daylight. Curves average realizations
611 in 10-minute bins by local time of day and are low pass filtered with a 1 hour time scale.
612

613 As cloud fraction decreases in the afternoon, transmissivity increases, reaching a
614 maximum of 0.7 at 13 local. Even though clouds decrease until 15 local, the transmissivity
615 decreases from 13, perhaps because clouds are more effective scatterers for lower solar
616 elevation angles. All-sky and partly cloudy transmissivity is similar to cloudy transmissivity,
617 because of the mostly cloudy conditions. Clear-sky conditional transmissivity is near unity,
618 but slightly less on average, perhaps because the narrow field of view of the ceilometer
619 classifies some partly cloudy scenes as clear. It is rare but possible for t to be greater than

620 unity, in the case that direct sunlight reaches the radiometer through gaps in clouds, while
621 the clouds scatter additional indirect sunlight into the radiometer.

622

623 Variability of downwelling radiation measured on the ship was linked to variation of the
624 clouds. The downwelling surface solar radiation S is the average of the clear-sky flux S_0
625 and the cloudy-sky flux S_1 weighted by the cloud fraction c ,

$$626 \quad S = (1 - c)S_0 + cS_1. \quad (1a)$$

627 The “maximum” cloud forcing

$$628 \quad S_1 - S_0 = (S - S_0)/c \quad (1b)$$

629 is the cloud forcing in the case that cloud fraction $c=1$ (Walsh and Chapman 1998). In
630 practice $(S - S_0)/c$ is subject to error when the cloud fraction is small.

631

632 Filled circles in Fig. 14a show mean downwelling solar radiative flux S for full-sky
633 conditions averaged in 2.5° longitude bins; filled circles in Fig. 14d show mean full-sky
634 longwave radiation. Boxes in Fig. 14 show sampling standard deviation as a measure of
635 variability within each longitude bin, and whiskers within the boxes show standard
636 deviation of the mean. The standard deviation of spatial and temporal variability sampled
637 by radiometers within a given longitude range is larger than the systematic zonal gradient
638 of solar radiation.

639

640 Open circles in Fig. 14 show mean clear-sky solar flux S_0 from the model of Iqbal (1988)
641 and clear-sky longwave radiative flux R_0 from the model of Hare (2005), parameterized
642 as surface water vapor, temperature, and latitude independent of the in situ radiative flux

643 observations. The clear-sky model simulates S_0 surface solar radiation in the absence of
644 clouds. All solar fluxes are zero at night. We average the solar flux over each local day to
645 average out instantaneous changes of S_0 due to the diurnal cycle of solar zenith angle. We
646 require at least 94% of samples to be available for a valid daylight average (5-19 hours
647 local). We then average over the entire day assuming zero solar radiation at night.
648 Longwave fluxes do not depend fundamentally on the solar cycle, so we use all 10-
649 minute means directly. Gray points in Fig. 14 show daily average solar radiation and 10-
650 minute average longwave radiation that are used for the longitude averages. Radiative
651 fluxes in Fig. 14b and e are shown only for times when the ceilometer 10-minute average
652 cloud fraction is overcast ($c=1$). Fluxes in Fig. 14c and f are shown only for clear
653 overhead ceilometer cloud fraction ($c=0$). The conditional average solar fluxes in Fig.
654 14b and c require some care not to alias the diurnal cycle.

655

656 Since the cloud fraction is not uniform throughout the day, the solar cycle of S_0 aliases
657 onto cloudy- or clear-sky conditional average solar fluxes. To avoid this we statistically
658 reconstruct cloudy-sky flux S_1 for non-cloudy times, and clear-sky flux S_0 for non-clear
659 times from the diurnal time-dependent conditional cloudy and clear-sky transmissivity,

660
$$\tilde{t}_1 = \langle t(c=1) \rangle^{\text{time}}$$

661
$$\tilde{t}_0 = \langle t(c=0) \rangle^{\text{time}},$$

662 where $\langle \rangle^{\text{time}}$ represents a diurnal composite as a function of the time of day.

663 Curves in Fig. 13 show the diurnal average solar transmissivity \tilde{t} (black), clear sky
664 transmissivity \tilde{t}_0 (magenta), cloudy-sky transmissivity \tilde{t}_1 (blue), and partially cloudy

665 transmissivity (gray). The diurnal cycle is composited on local time in 10-minute
666 intervals and low pass filtered to remove variability shorter than 1 hour.

667

668 The empirical reconstructions of cloudy and clear conditional solar fluxes are then the
669 product of the empirical transmissivity curves and S_0 derived from a clear-sky model:

$$670 \quad \tilde{S}_1 = \tilde{\tau}_1 S_0 \quad (2)$$

$$671 \quad \tilde{S}_0 = \tilde{\tau}_0 S_0.$$

672 The conditional clear- and overcast-sky solar flux reconstructions are suitable for
673 averaging daily without diurnal aliasing. Fig. 14b and c show daily mean reconstructions
674 averaged in longitude, $\langle\langle \tilde{S}_{\{0,1\}}^{\text{day}} \rangle\rangle^{\text{lon}}$. Since the sky is completely cloudy 67% of the
675 time, the cloudy conditional average is quite similar to the full-sky average. Overcast
676 solar fluxes (Fig. 14b) are approximately 25 W m^{-2} lower, and only half as variable as
677 compared to full-sky (Fig. 14a). Downwelling longwave fluxes in cloudy conditions are
678 10 W m^{-2} stronger than the full-sky average.

679

680 In clear conditions fluxes collapse approximately to the clear sky model (Fig. 14c,f).

681 Solar clear-conditional fluxes are slightly weaker than the clear sky model due to
682 undersampling of cloud fraction by the narrow field of view of the ceilometer. Clouds
683 undetected by the ceilometer reduce the solar radiation reaching the pyranometer. This
684 also explains average transmissivities less than 1 when the ceilometer detected clear skies
685 (Fig. 13). Longwave fluxes in clear conditions are statistically indistinguishable from the
686 clear sky model.

687

688 De Szoeke et al. (2010) find CMIP3 general circulation models all overestimate
689 downwelling solar radiation by at least 40 W m^{-2} in the region, partially compensated by
690 excessive net upwelling longwave radiation. We examine the effect of clouds on the
691 radiative fluxes by computing downwelling cloud radiative forcing from the methods and
692 data of Fig. 14. Incident solar cloud forcing $S-S_0$ is the difference between the observed
693 and modeled clear-sky downwelling solar and longwave radiation (Fig. 10a,d). Table 3
694 summarizes multi-cruise-year average radiative fluxes and cloud forcing for observations
695 within the region $18.5\text{-}21.5^\circ\text{S}$, $73.75\text{-}86.25^\circ\text{W}$ (all longitude bins along 20°S). Average
696 solar cloud forcing $S-S_0$ is -133 W m^{-2} .

697

698 We estimate maximum solar cloud forcing (MSCF) from the 1b and from the conditional
699 cloudy solar reconstruction S^*_1 (Table 3). Daily averaging $\langle S-S_0 \rangle$ and $\langle c \rangle$ before
700 dividing their quotient reduces problems associated with small denominators c and
701 prevents diurnal aliasing, but daily average $\langle c \rangle$ is not representative of the clouds
702 affecting the radiation. For example, about half the contribution to $\langle c \rangle$ is overnight while
703 $S-S_0$ is zero. Thus cloud fraction at night affects the maximum cloud forcing $\langle S-S_0 \rangle / \langle c \rangle$
704 even though it has no effect on the solar radiation. When instantaneous cloud fraction is
705 used instead, maximum cloud forcing estimates $(S-S_0)/c$ are ill conditioned by small or
706 zero cloud fraction c . In light of these problems we employ the conditionally
707 reconstructed cloudy sky flux S^*_1 to get the maximum cloud forcing. Reconstructed S^*_1 is
708 likely to be representative of all clouds because of the large number of fully cloudy
709 realizations composited in the conditional cloudy reconstruction.

710

711 The research cruise in 2004 took place in December, later in the seasonal cycle than the
712 other cruises in October-November. Observed and modeled solar fluxes are comparable
713 (within 10 W m^{-2}) between the 2004 December cruise and the other years. However,
714 cloud fraction is considerably less in December, and the increased number of clear
715 observations make maximum cloud forcings calculated from 1b unreliable. This method
716 estimates a physically absurd average cloud forcing of -488 W m^{-2} for 2004 December,
717 impossibly 100 W m^{-2} stronger than the clear-sky solar flux. The conditionally
718 reconstructed cloud forcing $\tilde{S}_1 - S_0$ is minimally affected by removing December data
719 from the all-cruise average because the conditional reconstruction of transmissivity and
720 hence \tilde{S}_1 are representative of October-November conditions. We suspect \tilde{S}_1 is not
721 representative of clouds in December, and there are not enough cloudy data in December
722 2004 to make an independent radiative reconstruction for that season. Thus 2004
723 December reconstructed maximum solar cloud forcings $\tilde{S}_1 - S_0$ in Table 3 and $\tilde{R}_1 - R_0$ in
724 Table 4 may be too weak to explain the stronger cloud forcing (even when there were
725 fewer clouds) in December.

726

727 Surface thermal longwave cloud forcing is about $+60 \text{ W m}^{-2}$ (Table 4). While small cloud
728 fraction is still a problem, longwave radiation has a weak diurnal cycle and so is not
729 subject to diurnal aliasing effects. The empirical longwave \tilde{R}_1 is simply the conditional
730 average for cloudy skies. Because the diurnal variability is weak, daily average cloud
731 fraction is representative, so $\langle R - R_0 \rangle / \langle c \rangle$ is a good estimate of maximum longwave cloud
732 forcing (MLCF). MLCF computed this way and from the conditional cloudy sky
733 radiation $\tilde{R}_1 - R_0$ agree well, at about 70 W m^{-2} .

734

735 Surface longwave radiation is strongly correlated with the amount of clouds, indicating
736 variations in emission of the clear atmosphere and in cloud brightness temperature only
737 weakly influence the downwelling radiation. Figure 15, a scatter plot of surface
738 downwelling longwave radiation versus cloud fraction, suggests surface longwave
739 radiation is a sum of clear sky and a nearly constant maximum cloud forcing weighted by
740 the cloud fraction,

$$741 \quad R = R_0 + c(R_1 - R_0). \quad (3)$$

742 Small dots in Fig. 15 indicate cloud fractions of 0 or 1. Radiative forcing for partial cloud
743 fraction lies on a mixture line between clear and cloudy end points. Cloud fraction
744 explains 75% of the variance of downwelling longwave radiation. Modeled clear-sky
745 longwave radiation explains only 16% of the variance of observed radiation in clear
746 conditions. Clouds undetected by the narrow-beam ceilometer modify longwave radiation
747 from its clear-sky value. Only approximately 10% of the surface longwave radiation
748 variance could be explained by variations in emission from the bases of the clouds
749 themselves. Considering this insignificant fraction of variance, it is not surprising that
750 cloud base brightness temperature estimated from the longwave radiation is uncorrelated
751 with ceilometer cloud base height retrievals. Apparently slight changes in either the clear-
752 sky or cloud radiance temperatures have only a small effect on the longwave radiation,
753 while cloud fraction modulates the large difference between clear and cloudy longwave
754 radiation.

755

756 We show daily mean longwave and solar cloud radiative forcing against daily mean
 757 cloud fraction in Fig. 16. Daily mean cloud fraction is mostly greater than 0.88 and
 758 always greater than 0.3. As expected from the strong correlation of 10-minute mean
 759 downwelling longwave radiation to cloud fraction (Fig. 15), and from relatively constant
 760 clear-sky downwelling longwave radiation, daily cloud fraction explains daily mean
 761 longwave cloud forcing well (Fig. 16, open circles). Cloud forcing is the product of the
 762 maximum cloud forcing and the cloud fraction; for longwave radiation, $R-R_0 = c(R_1-R_0)$.
 763 Assuming the maximum cloud forcing is constant, we model the effect of cloud fraction
 764 on the cloud radiative forcing with straight lines connecting the maximum longwave and
 765 solar cloud forcing at $c=1$ to zero cloud forcing for $c=0$. The correlation of daily
 766 longwave cloud forcing with cloud fraction is $r=0.93$.

767

768 Daily solar cloud radiative forcing is explained less well by daily cloud fraction (dots)
 769 than longwave cloud forcing, with a correlation coefficient of only $r=-0.76$. The solar
 770 cloud forcing in Fig. 16 suggests a nonlinear dependence on cloud fraction, with stronger
 771 maximum cloud forcing on days when there is more cloud fraction. The nonlinear
 772 dependence on cloud fraction is explained by considering cloud forcing as a product of
 773 cloud fraction, transmissivity, and clear-sky solar radiation:

$$774 \quad S - S_0 = c(S_1 - S_0) = c(t_1 - 1)S_0. \quad (4)$$

775 Solar cloud forcing depends nonlinearly on daily mean cloud fraction because of the
 776 negative correlation of c with S_0 due to afternoon clearing during strong clear-sky solar
 777 radiation. The solar-weighted daily cloud fraction, $c_s = \langle S_0 c \rangle / \langle S_0 \rangle$ is more
 778 representative of the cloud fraction when solar radiation is actually incident. Solar-

779 weighted daily cloud fraction is usually less than ordinary cloud fraction because most
780 clearing is observed in the afternoon (Fig. 8). Crosses in Fig. 16 show somewhat more
781 linear dependence of solar cloud radiative forcing on the solar-weighted cloud fraction
782 compared to ordinary cloud fraction. The correlation coefficient of solar cloud forcing
783 with solar-weighted cloud fraction is $r=-0.83$. Additionally, stratocumulus clouds are
784 expected to be more opaque when cloud fraction is higher and geometrically and
785 optically thinner when they are more patchy and clearing. This negative correlation of
786 cloud fraction c and transmissivity t_1 also results in nonlinear dependence of cloud
787 forcing on cloud fraction in (4). Straight lines in Fig. 16 connect zero cloud forcing to the
788 maximum cloud forcing from Table 4.

789

790 We compare daily mean solar and longwave cloud forcing in the cloud forcing phase
791 diagram of Fig. 17. Filled circles are from October-November cruises to the 20°S, 75-
792 85°W region. We assume there is zero longwave and solar cloud forcing when there are
793 no clouds, and therefore the model line (black) extends from the origin to the average
794 maximum cloud forcing, as in Fig. 16. Our observations agree with the regression line
795 from 4 years of buoy observations at 20°S, 85°W (Cronin et al. 2006), and fall in the
796 stratocumulus and trade cumulus region of the cloud-forcing phase space (Fairall et al.
797 2008). Even for October-November, when the cloud regime is strongly stratocumulus,
798 observed cloud forcing falls in a wide range of the solar-longwave phase space. Daily
799 average cloud forcing from outside the 20°S region (crosses), or from December (circles)
800 do not show significantly different solar vs. longwave cloud forcing behavior.

801

802 **6. Surface Cloud Forcing in General Circulation Models**

803 Solar radiation is the only warming term over most of the ocean. Longwave radiation
804 damps SST anomalies. Cloud radiative forcing modulates solar and longwave radiation,
805 and is an important term in the upper ocean heat budget, especially beneath the extensive
806 tropical stratocumulus cloud decks. De Szoeké et al. (2010) ranked models by solar
807 radiation absorbed by the ocean. Here we focus specifically on attributing model
808 radiative forcing anomalies to errors in cloud radiative forcing. We evaluate cloud
809 radiative forcing in ocean-atmosphere coupled general circulation models (GCMs) from
810 the third Coupled Model Intercomparison Project (CMIP3) with the cloud radiative
811 forcing observed along 20°S from the 7 years of cruises.

812

813 Since the surface heat budget responds to the net radiative heat flux, surface cloud
814 forcing is reduced slightly by surface absorption coefficients. For longwave this is the
815 emissivity of the sea surface $\epsilon_s=0.97$; for solar radiation it is the complement of the
816 surface albedo $1-\alpha_s=0.945$. Thus net longwave and solar cloud forcings are respectively
817 defined,

$$818 \text{LCF} = \epsilon_s(R - R_0)$$

$$819 \text{SCF} = (1 - \alpha_s)(S - S_0).$$

820

821 Figure 18 compares surface longwave and shortwave cloud forcing climatology for
822 October-November from 15 CMIP3 coupled GCMs with the ship observations. In situ
823 observations from the WHOI buoy at 20°S, 85°W (Cronin et al. 2006), remote sensing
824 from the ISCCP Flux Data set, and the 7 years of ship observations agree well. For the

825 ISCCP FD and Stratus buoy data sets we use MODIS cloud fraction (Fig. 1). Surface
826 solar cloud forcing in all CMIP3 models (-20 to -90 W m^{-2}) lacks the observed strength ($-$
827 120 W m^{-2}). Longwave cloud forcing offsets about 50% of solar cloud forcing for
828 observations and for the consensus of models. Longwave errors offset solar errors in the
829 same proportion. Correlated among models at $r=-0.63$, longwave cloud forcing errors
830 compensate about half of shortwave cloud forcing errors. Two models have 60 W m^{-2}
831 too-weak surface solar cloud forcing, yet have longwave cloud forcing close to the
832 observed, resulting in 60 W m^{-2} too much downwelling radiation absorbed at the surface.
833

834 Surface cloud forcing errors are associated with deficiencies of cloud fraction. Model
835 longwave and solar cloud forcing are correlated to cloud fraction at 0.82 and -0.72 . The
836 models mimic the proportionality of cloud forcing to cloud fraction (Fig. 18), falling near
837 the line between the observed cloud forcing and cloud fraction and zero cloud forcing for
838 clear skies. This suggests that simulated clouds have the right cloud forcing when
839 present, but too few clouds in the models result in too little cloud forcing cooling.
840

841 **7. Summary**

842 Models have too strong net radiation because they have too few clouds. On the whole,
843 simulated clouds have approximately the right cloud radiative forcing when present.
844 Longwave cloud forcing offsets 50% of shortwave cloud forcing in observations.
845 Conveniently longwave cloud forcing error also offsets 50% of shortwave cloud forcing
846 error in models. In CMIP3 models, errors in cloud amount dominate any errors that could
847 be attributed to cloud albedo or aerosol indirect effect issues.

848

849 Observations show that daily average downwelling longwave radiation and longwave
850 cloud forcing are proportional to the cloud amount, indicating relatively constant
851 maximum longwave cloud forcing, i.e. constant radiation from clouds when present.
852 Surface solar radiative forcing responds linearly to cloud amount to some degree, but has
853 a nonlinear tendency for stronger solar radiative forcing at higher cloud fraction, partly
854 explained by clearing during high clear-sky solar flux in the afternoon.

855

856 Daily solar cloud forcing along 20°S falls within a wide range about the stratocumulus
857 regime ($|S-S_0| = 2(R-R_0)$) of the longwave-solar forcing phase diagram (Fairall et al.
858 2008). The range stretches from the warmer trade cumulus regime ($|S-S_0| = 3(R-R_0)$) to
859 the cooler midlatitude cloud regime, with a relatively smaller proportion of solar to
860 longwave cloud forcing. The 20 days with anomalously low ratio of solar to longwave
861 cloud forcing ($|S-S_0| < 2(R-R_0) - 10 \text{ W m}^{-2}$) have about 50 W m^{-2} weaker maximum solar
862 cloud forcing but almost no change in their longwave cloud forcing (gray symbols, Fig.
863 16). A 3% decrease in their median cloud fraction accounts for some of the reduction in
864 solar forcing, and the reduction in solar forcing is amplified because the reduction of
865 clouds is mostly in the afternoon.

866

867 The midlatitudes have colder atmosphere and weaker solar radiation than the tropics.
868 Clear periods between midlatitude storms correspond to cold, dry, descending air and less
869 emissive atmospheric conditions. The relative increase in surface longwave cloud forcing
870 puts the storm tracks in the $|S-S_0| < 2(R-R_0) - 10 \text{ W m}^{-2}$ region of the cloud forcing phase

871 diagram (Fig. 17). Unlike midlatitude clouds, the tropical stratocumulus clouds observed
872 in this study have weaker solar maximum cloud forcing than typical stratocumulus and
873 similar longwave cloud forcing. This might result from tenuous clouds that allow a large
874 amount of solar radiation through but are nevertheless strongly emissive in the thermal
875 infrared.

876

877 The effects of aerosols on the solar radiation could account for some variance in the solar
878 cloud forcing, perhaps explaining deviations from the typical stratocumulus cloud-forcing
879 phase space regime (Fig. 17). Overestimation of the clear sky solar flux by not
880 considering the aerosol direct effect diminishing clear sky radiation would result in
881 overestimation of our solar cloud forcing. Cloud albedo aerosol indirect effect (Twomey
882 1974) affects solar flux measured by the solar radiometers, increasing the strength and
883 variability of the solar cloud forcing, accounting for more variance from the
884 stratocumulus regime in the cloud forcing phase space.

885

886 Thermodynamic atmospheric soundings are remarkably constant over the 7 years of
887 research cruises to 20°S. A 14-level idealized sounding based on 487 soundings along
888 20°S is available for model studies (Table 1).

889

890 Cloud base-LCL displacement is a thermodynamic index of decoupling. This
891 displacement increases both westward with longitude, and during the daylight hours, as
892 summarized by the schematic of Fig. 19. Larger displacements of 500-1000 m also grow
893 increasingly common to the west. Afternoon CB-LCL displacement is 400 m greater than

894 the displacement at night. The westward rise of cloud base coincides with higher and
895 more variable CB-LCL displacement. For deep subcloud layers in the afternoon, cloud
896 base is less likely to be found near the LCL.

897

898 Jones et al. (2011) find decoupling is correlated to cloud thickness. For all 20°S
899 observations we find cloud top height, cloud base height, and LCL to be correlated (Table
900 5). Cloud top and cloud base height, correlated at $r=0.7$, both explain CB-LCL
901 displacement, cloud base more so than cloud top (CB-LCL depends explicitly on CB).
902 Cloud top height does not explain any additional variance in the CB-LCL displacement,
903 but it is consistent with deeper boundary layers being more decoupled. The gradient in
904 longitude explains some but not all of the variance in cloud top, cloud base, LCL, and
905 CB-LCL displacement.

906

907 Semidiurnal cycles of variables related to boundary layer height are observed at 75°W,
908 but not 85°W. Lag correlations of diurnal cycles in the ship data do not show coherent
909 propagation from 75° to 85°W. Moreover the phase of such tropospheric gravity waves is
910 not consistent with constructive interference with the local diurnal cycle at 75°W and
911 destructive interference at 85°W. Other mechanisms by which the semidiurnal cycle in
912 variables related to boundary layer height can weaken at 85°W relative to 75°W include
913 dissipation of waves as they propagate offshore, and spatial interference of diurnally-
914 forced waves emitted from different source locations, e.g. from the Peruvian and Chilean
915 Andes on either side of the Arica Bight. Though the ship data provide excellent time
916 resolution of the diurnal cycle, the spatial sampling of the composites is rather coarse.

917 Satellite observations may be able to resolve spatial interference from the waves.
918 Stability in the inversion is an effective waveguide for tropospheric gravity waves.
919 Energy of waves traveling along the inversion could be dissipated by entrainment mixing
920 free tropospheric air into the boundary layer at the inversion.

921

922 **Acknowledgement**

923 The United States National Oceanic and Atmospheric Administration (NOAA) Climate
924 Prediction Program for the Americas/Earth System Science program (CPPA/ESS) has
925 supported this work, including the shipboard observations for VOCALS regional
926 experiment (grant GC09-507. MODIS data were downloaded from the NASA web site,
927 <http://modis.gsfc.nasa.gov/>. We acknowledge the modeling groups, the Program for
928 Climate Model Diagnosis and Intercomparison (PCMDI), and the WCRP's Working
929 Group on Coupled Modelling (WGCM) for their roles in making available the WCRP
930 CMIP3 multi-model dataset. Support of the CMIP3 data set is provided by the Office of
931 Science, U.S. Department of Energy. Data provided by the UK Met Office Hadley Centre
932 are under Crown copyright, 2005. We would like to thank the crew and scientists aboard
933 the NOAA R/V *Ronald H. Brown* and the UNOLS R/V *Roger Revelle* during the
934 research cruises when we collected these measurements, and Dr. Peter Minnett for the
935 use of his microwave radiometer in 2008. We thank Sergio Pezoa, Dan Wolfe, Ludovic
936 Bariteau, and Dan Gottas for their continual development and maintenance of the
937 shipboard NOAA PSD meteorology and flux measurement systems.

938

939 **References**

940 Albrecht, B. A., 1989: Aerosols, Cloud Microphysics, and Fractional Cloudiness.
941 *Science*, **245**, 1227-1230.

942 Bretherton, C. S., and M. C. Wyant, 1997: Moisture Transport, Lower-Tropospheric
943 Stability, and Decoupling of Cloud-Topped Boundary Layers. *J. Atmos. Sci.*, **54**, 148-
944 167, 10.1175/1520-0469(1997)054<0148:mtltsa>2.0.co;2.

945 Bretherton, C. S., R. Wood, R. C. George, D. Leon, G. Allen, and X. Zheng, 2010:
946 Southeast Pacific stratocumulus clouds, precipitation and boundary layer structure
947 sampled along 20°S during VOCALS-REx. *Atmos. Chem. Phys.*, **10**, 10639-10654,
948 10.5194/acp-10-10639-2010.

949 Colbo, K., and R. Weller, 2007: The variability and heat budget of the upper ocean under
950 the Chile-Peru stratus. *J. Mar. Res.*, **65**, 607-637.

951 Comstock, K. K., R. Wood, S. E. Yuter, and C. S. Bretherton, 2004: Reflectivity and rain
952 rate in and below drizzling stratocumulus. *Quart. J. Roy. Met. Soc.*, **130**, 2891-2918,
953 10.1256/qj.03.187.

954 Comstock, K. K., S. E. Yuter, R. Wood, and C. S. Bretherton, 2007: The Three-
955 Dimensional Structure and Kinematics of Drizzling Stratocumulus. *Mon. Wea. Rev.*,
956 **135**, 3767-3784, doi:10.1175/2007MWR1944.1.

957 Cronin, M. F., N. A. Bond, C. W. Fairall, and R. A. Weller, 2006: Surface Cloud Forcing
958 in the East Pacific Stratus Deck/Cold Tongue/ITCZ Complex. *J. Climate*, **19**,
959 392-409.

960 Davey, M. K., and Coauthors, 2002: STOIC: a study of coupled model climatology and
961 variability in tropical ocean regions. *Climate Dynamics*, **18**, 403-420.

962 de Szoeke, S. P., and S.-P. Xie, 2008: The tropical eastern Pacific seasonal cycle:
963 Assessment of errors and mechanisms in IPCC AR4 coupled ocean-atmosphere
964 general circulation models. *J. Climate*, **21**, 2573-2590.

965 de Szoeke, S. P., S. E. Yuter, P. Zuidema, C. W. Fairall, and W. A. Brewer, 2010: Ship-
966 based observation of drizzling stratocumulus cloud from EPIC to VOCALS. *CLIVAR*
967 *Exchanges*, **15**, 11-13.

968 Fairall, C. W., T. Uttal, D. Hazen, J. Hare, M. F. Cronin, N. Bond, and D. E. Veron,
969 2008: Observations of cloud, radiation, and surface forcing in the equatorial eastern
970 Pacific. *J. Climate*, **21**, 655-673.

971 Garreaud, R. D., and R. C. Muñoz, 2005: The Low-Level Jet off the West Coast of
972 Subtropical South America: Structure and Variability. *Mon. Wea. Rev.*, **133**, 2246-
973 2261, 10.1175/mwr2972.1.

974 Hare, J., C. Fairall, T. Uttal, D. Hazen, M. F. Cronin, N. Bond, and D. Veron, 2005:
975 Cloud, radiation, and surface forcing in the equatorial eastern Pacific. NOAA
976 Technical Memorandum OAR PSD-307.

977 Iqbal, M., 1988: Spectral and total sun radiance under cloudless skies. *Physical*
978 *Climatology for Solar and Wind Energy*, R. Guzzi, and C. G. Justus, Eds., World
979 Scientific, 196–242.

980 Jones, C. R., C. S. Bretherton, and D. Leon, 2011: Coupled vs. decoupled boundary
981 layers in VOCALS-REx. *Atmos. Chem. Phys.*, **11**, 7143-7153, 10.5194/acp-11-7143-
982 2011.

983 Klein, S. A., and D. L. Hartmann, 1993: The seasonal cycle of low stratiform clouds. *J.*
984 *Climate*, **6**, 1588-1606.

985 Kollias, P., C. W. Fairall, P. Zuidema, J. Tomlinson, and G. A. Wick, 2004: Observations
986 of marine stratocumulus in SE Pacific during the PACS 2003 cruise. *Geophys. Res.*
987 *Lett.*, **31**, L22110, 10.1029/2004gl020751.

988 Mechoso, C. R., and Coauthors, 1995: The seasonal cycle over the tropical Pacific in
989 coupled ocean-atmosphere general circulation models. *Mon. Wea. Rev.*, **123**, 2825-
990 2838.

991 Moran, K. P., and Coauthors, 2011: A motion stabilized W-band radar for shipboard
992 cloud observations and airborne studies of sea spray. *Journal of Boundary Layer*
993 *Meteorology*.

994 O'Dell, C. W., F. J. Wentz, and R. Bennartz, 2008: Cloud Liquid Water Path from
995 Satellite-Based Passive Microwave Observations: A New Climatology over the
996 Global Oceans. *J. Climate*, **21**, 1721-1739.

997 Platnick, S., M. D. King, S. A. Ackerman, W. P. Menzel, B. A. Baum, J. C. Riedi, and R.
998 A. Frey, 2003: The MODIS cloud products: algorithms and examples from Terra.
999 *IEEE Transactions on Geoscience and Remote Sensing*, **41**, 459-473.

1000 Rahn, D. A., and R. Garreaud, 2010: Marine boundary layer over the subtropical
1001 southeast Pacific during VOCALS-REx ,Äi Part 1: Mean structure and diurnal cycle.
1002 *Atmos. Chem. Phys.*, **10**, 4491-4506, 10.5194/acp-10-4491-2010.

1003 Risien, C. M., and D. B. Chelton, 2008: A Global Climatology of Surface Wind and
1004 Wind Stress Fields from Eight Years of QuikSCAT Scatterometer Data. *J. Phys.*
1005 *Oceanogr.*, **38**, 2379-2413.

1006 Tomlinson, J. M., R. Li, and D. R. Collins, 2007: Physical and chemical properties of the
1007 aerosol within the southeastern Pacific marine boundary layer. *J. Geophys. Res.*, **112**,
1008 D12211, 10.1029/2006jd007771.

1009 Twomey, S., 1974: Pollution and the planetary albedo. *Atmospheric Environment (1967)*,
1010 **8**, 1251-1256.

1011 Wood, R., and Coauthors, 2011: The VAMOS Ocean-Cloud-Atmosphere-Land Study
1012 Regional Experiment (VOCALS-REx): goals, platforms, and field operations.
1013 *Atmospheric Chemistry and Physics Discussions*, **11**, 627-654, doi:10.5194/acpd-10-
1014 20769-2010.

1015 Xie, S.-P., 2004: The shape of continents, air-sea interaction, and the rising branch of the
1016 Hadley circulation. *The Hadley Circulation: Past, Present and Future*, H. F. Diaz,
1017 and R. S. Bradley, Eds., Kluwer Academic Publishers, 121-152.

1018 Zuidema, P., E. R. Westwater, C. Fairall, and D. Hazen, 2005: Ship-based liquid water
1019 path estimates in marine stratocumulus. *J. Geophys. Res.*, **110**,
1020 10.1029/2005jd005833.

1021 Zuidema, P., D. Painemal, S. de Szoeko, and C. Fairall, 2009: Stratocumulus Cloud-Top
1022 Height Estimates and Their Climatic Implications. *J. Climate*, **22**, 4652-4666,
1023 doi:10.1175/2009JCLI2708.1.

1024

1025 **List of Figures**

1026 Figure 1. October-November satellite sea surface temperature (SST) and cloud fraction
1027 climatology in the southeastern tropical Pacific Ocean from the AMSR-E and MODIS
1028 instruments, respectively. Colored lines indicate tracks of NOAA research cruises

1029 included in the stratocumulus synthesis data set. Dates of reaching stations at 75° and
1030 85°W are listed for each track in the key below.

1031

1032 Figure 2. Eight sounding cross-sections of potential temperature and specific humidity in
1033 the troposphere below 2.5 km along 20°S. Red points indicate lifting condensation level,
1034 blue points ceilometer cloud base height. Crosses show the inversion diagnosed from the
1035 temperature minimum for each sounding, magenta lines show the inversion diagnosed
1036 from remote sensing.

1037

1038 Figure 3. Thermodynamic variables relative humidity (RH), temperature (T), water vapor
1039 specific humidity (q_v), and potential temperature in and above the marine atmospheric
1040 boundary layer for 487 soundings along 20°S, 75-85°W. Dots are the mode of the
1041 distribution for each level, solid line is the median, and dashed line is the mean.

1042

1043 Figure 4. Zonal (u) and meridional (v) wind distributions with height (shades), and
1044 median wind profile (black line) from the 20°S soundings. Dashed lines indicate the
1045 sampling standard deviation of wind profiles.

1046

1047 Figure 5. (a) Mean cloud boundaries from ship remote sensing observations (gray boxes).
1048 Lifting condensation level (LCL) for a parcel with surface humidity and temperature
1049 (black lines). Unfilled boxes show mean plus and minus one standard deviation of the
1050 mean. (b) Cloud fraction (gray) and LWP (black) with whiskers indicating standard
1051 deviation of the mean.

1052

1053 Figure 6. (a) Accumulation mode aerosol concentration (cm^{-3} , $D > 0.1 \times 10^{-6}$ m) along
1054 20°S vs. longitude. Circles and whiskers show mean and standard deviation of the mean
1055 west and east of 80°W . (b) Histogram of concentrations in 25 cm^{-3} bins sampled by
1056 TAMU in 2003-2004; and (c) histogram for the Lasair-II in 2005-2007. Dots show 10-
1057 minute LWP observations; circles and whiskers show LWP mean and standard deviation
1058 of the mean for 25 cm^{-3} bins.

1059

1060 Figure 7. (a) Fraction of sky with reflectivity above a threshold, excluding noise. (b)
1061 Probability density as the fraction of full sky per bin (width 2 dBZ or $0.0175 \text{ km}^{-1} \text{ sr}^{-1}$) on
1062 a logarithmic scale. Vertically pointing instruments such as the W-band cloud radar (dot-
1063 dashed), millimeter cloud radar (MMCR, gray), and ceilometer (triangles) are compared
1064 to the C-band scanning radar (solid black). The threshold for the ceilometer is in optical
1065 backscatter units ($\text{km}^{-1} \text{ sr}^{-1}$, top axis).

1066

1067 Figure 8. (a) Diurnal cycle of cloud fraction (triangles) for 20°S $75\text{-}85^\circ\text{W}$. Dark gray area
1068 corresponds to the fraction of samples with cloud fraction $c=1$, white for $c=0$, light gray
1069 for $0 < c < 1$. (b) Diurnal composite mean cloud base and top height (shaded), and cloud
1070 thickness (black line). (c) Liquid water path (LWP) mean (circles) and 15, 30, 50, 70, and
1071 85th percentiles. The region 30-70th percentile region is shaded. Squares show vertical
1072 average liquid water content (LWC) in the cloud for all sky (black) and cloudy (gray)
1073 conditions.

1074

1075 Figure 9. Diurnal cycle of vertical displacement of cloud base height from LCL (CB-
1076 LCL) for (a) all longitudes, (b) 85°W, (c) 80°W, and (d) 75°W as in Table 1. Shaded
1077 squares show relative frequency in each panel, circles indicate the mode of the
1078 distribution. Black lines on the left show normalized probability distributions for all
1079 hours. The diurnal cycle is repeated over 1.5 days.

1080

1081 Figure 10. Diurnal cycle scatter plot of cloud base height vs. LCL in four 6-hour increments,
1082 0-6, 6-12, 12-18, and 18-24 hours local (rows); at three longitudes, (a-d) 85°W, (e-h) 80°W,
1083 and (i-l) 75°W, 20°S (columns). Black dots indicate coincident 10-minute LCL and cloud
1084 base height observations. Shaded squares show joint frequency of LCL and cloud base in
1085 50x50 m² bins.

1086

1087 Figure 11. (a-f) Longitude-solar time Hovmöller diagrams of boundary layer and cloud
1088 variables along 20°S. Dotted lines show propagation speed for 30 m s⁻¹ propagation.
1089 Diurnal cycles of (g) cloud top height, (h) liquid water path, and (i) water vapor path at
1090 85°W (bold) and 75°W. Dashed lines show the first diurnal harmonic. The diurnal cycle
1091 is repeated over 36 hours.

1092

1093 Figure 12. (a-f) Fraction of variance explained by the first diurnal (dark) and semidiurnal
1094 (light gray) components at 85° and 75°W. (g-i) Lag correlation between 75° and 85°W
1095 (bold), and autocorrelations at 85°W (solid) and 75°W (dashed). Positive lag indicates
1096 75°W leads 85°W.

1097

1098 Figure 13. Daylight variation of solar transmission fraction. Magenta dots are for

1099 ceilometer cloud fraction of zero, blue dots are for ceilometer cloud fraction of 1. Black
1100 crosses show transmission for cloud fraction between 0 and 1. Solid lines show the mean
1101 composited on the time of day. [~/Data/Stratus/20s/sw_frac.eps]

1102

1103 Figure 14. Solar and longwave surface downwelling radiation measured along 20°S
1104 (filled circles) and simulated with a clear-sky model (open circles) in October-November.
1105 Full-sky values (a,d); Cloudy conditions (b,e) with ceilometer $c=1$; clear conditions (c,f)
1106 $c=0$. Boxes indicate the sampling standard deviation, whiskers the standard deviation of
1107 the mean.

1108

1109 Figure 15. Downwelling longwave radiation vs. cloud fraction for fully clear or cloudy
1110 (dots), and partially cloudy skies (circles) in October-November along 20°S. Gaussian
1111 random numbers have been added to cloud fractions of 0 or 1 to visualize the distribution.

1112

1113 Figure 16. Daily mean cloud radiative forcing as a function of cloud fraction: solar (dots
1114 and crosses) and longwave (open circles). Crosses show insolation-weighted cloud
1115 fraction for solar cloud radiative forcing. Gray points identify the condition $|S-S_0| < 2(R-$
1116 $R_0) - 10 \text{ W m}^{-2}$.

1117

1118 Figure 17. Longwave versus solar cloud forcing phase diagram of daily averages at 20°S,
1119 75-85°W in October-November (filled circles), 20°S December (open circles), and
1120 outside the 20°S region (crosses). The black line intersects the maximum cloud forcing
1121 (large cross) in Tables 2 and 3. Cloud forcing regressions for stratocumulus and trade

1122 cumulus regimes (gray, Fairall et al. 2008), and the regression at the Stratus buoy
1123 (dashed, Cronin 2006) are shown.

1124

1125 Figure 18. Surface longwave and solar cloud forcing observed (circles) and simulated by
1126 coupled GCMs. Cloud fraction for the Stratus buoy and ISCCP FD are provided by
1127 MODIS satellite retrievals.

1128

1129 Figure 19. Schematic of the mean longitude structure and diurnal cycle (repeated 3 times)
1130 of the marine boundary layer and stratocumulus clouds along 20°S, 85-75°W. Turbulent
1131 surface fluxes are presented in de Szoeke et al. (2010).

1132

1133 **List of Tables**

1134 Table 1. Idealized 14-level tropical eastern Pacific sounding from 487 rawinsondes along
1135 20°S.

1136

1137 Table 2. Total and minimum diurnal (per local hour) sampling for the composite 20°S
1138 transect.

1139

1140 Table 3. Mean surface clear-sky solar radiation, solar radiation, cloud forcing, and
1141 estimates of maximum cloud forcing \pm the standard error of the mean (W m^{-2}). Angle
1142 brackets indicate daily averages. Columns show the average for all 7 years of cruises, the
1143 average for the 6 years of cruises in October-November, and the average of the cruise in
1144 2004 December. Standard errors of the mean less than the least significant digit (e.g. 1 W
1145 m^{-2}) are not listed.

1146

1147 Table 4. Surface longwave clear-sky radiation, longwave radiation, cloud forcing, and
1148 estimates of maximum cloud forcing (W m^{-2}) as in Table 2.

1149

1150 Table 5. Correlations of cloud geometry: cloud top, cloud base (CB), lifting condensation
1151 level (LCL), cloud thickness (top-CB), and CB-LCL displacement. Correlations weaker
1152 than 0.3 (shaded) do not differ from zero with 95% statistical significance, assuming an
1153 autocorrelation time scale of 6 hours for 43 degrees of freedom.

1154

Figures

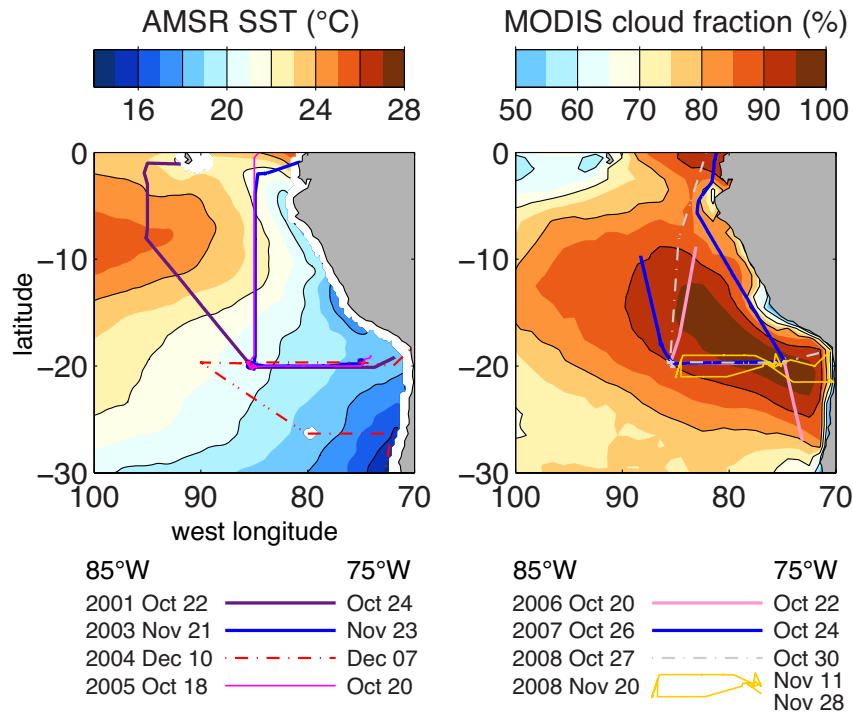


Figure 1. October-November satellite sea surface temperature (SST) and cloud fraction climatology in the southeastern tropical Pacific Ocean from the AMSR-E and MODIS instruments, respectively. Colored lines indicate tracks of NOAA research cruises included in the stratocumulus synthesis data set. Dates of reaching stations at 75° and 85°W are listed for each track in the key below.

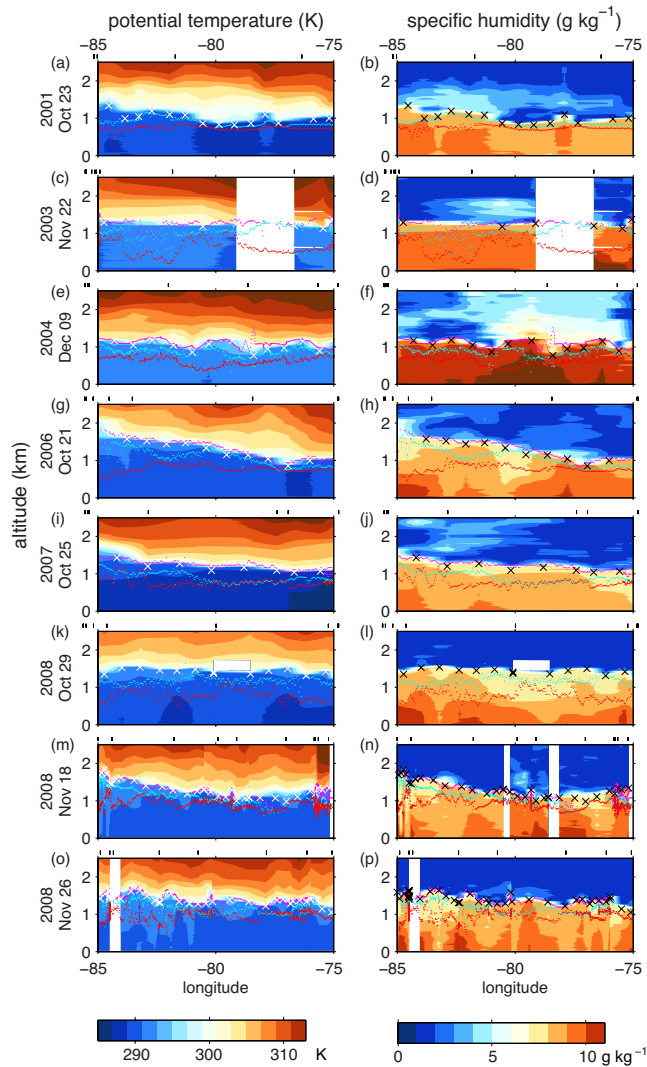


Figure 2. Eight sounding cross-sections of potential temperature and specific humidity in the troposphere below 2.5 km along 20°S. Red points indicate lifting condensation level, blue points ceilometer cloud base height. Crosses show the inversion diagnosed from the temperature minimum for each sounding, magenta lines show the inversion diagnosed from remote sensing.

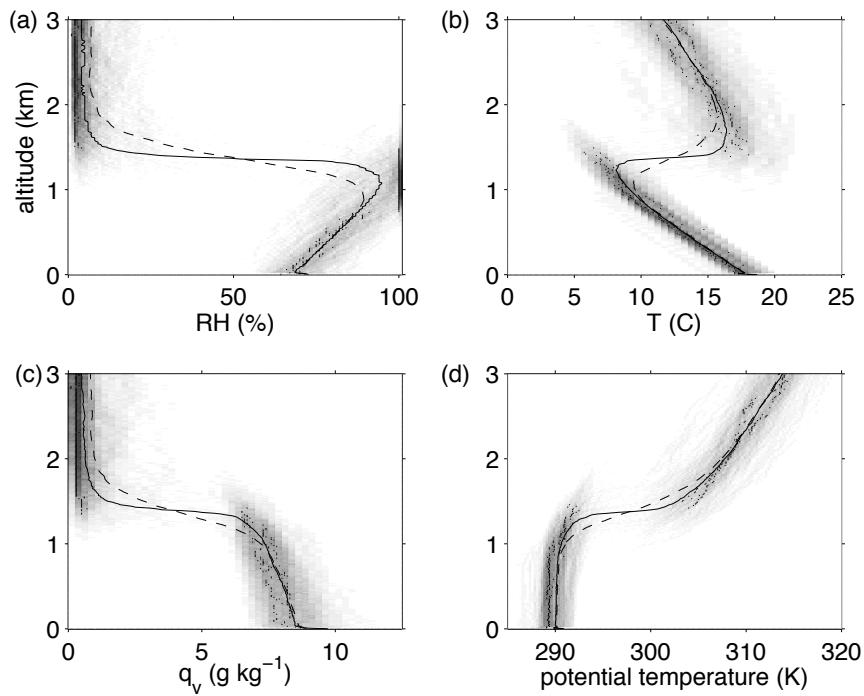


Figure 3. Thermodynamic variables relative humidity (RH), temperature (T), water vapor specific humidity (q_v), and potential temperature in and above the marine atmospheric boundary layer for 487 soundings along 20°S , $75\text{-}85^\circ\text{W}$. Dots are the mode of the distribution for each level, solid line is the median, and dashed line is the mean.

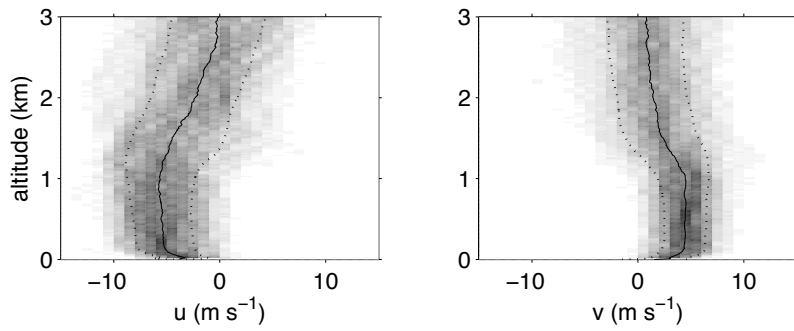


Figure 4. Zonal (u) and meridional (v) wind distributions with height (shades), and median wind profile (black line) from the 20°S soundings. Dashed lines indicate the sampling standard deviation of wind profiles.

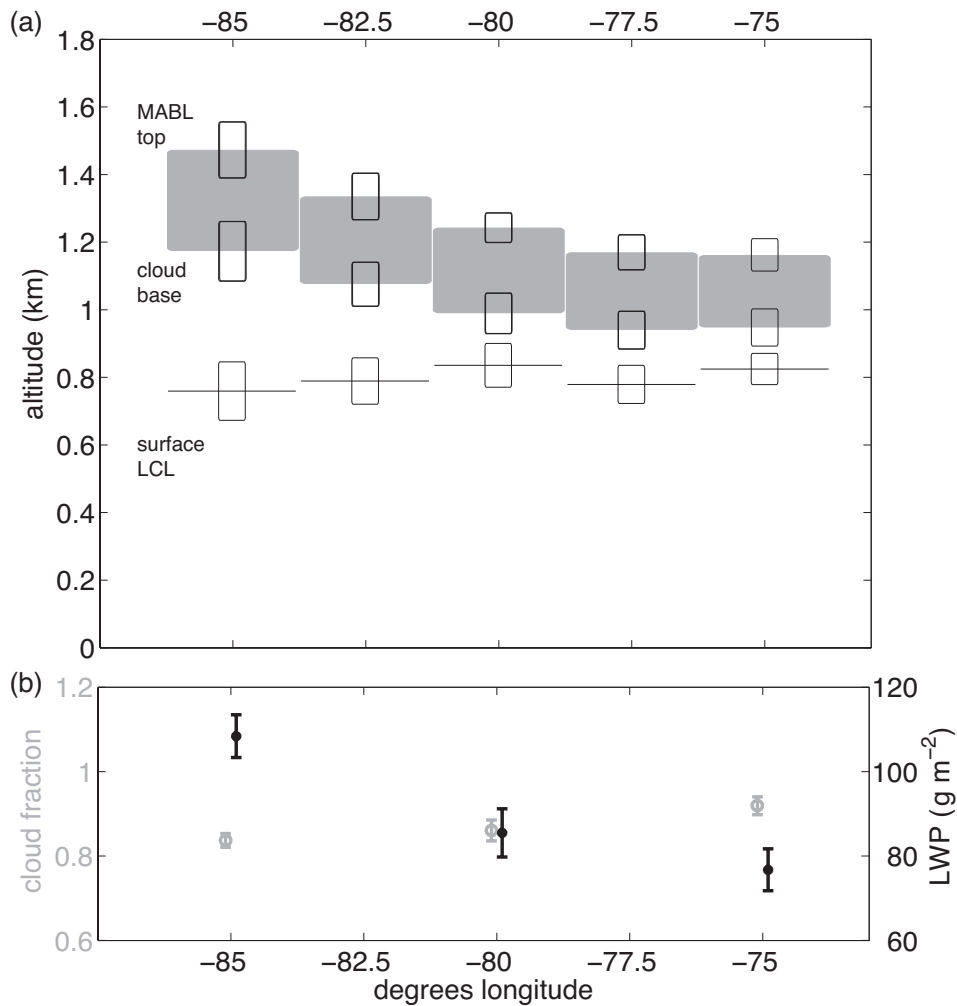


Figure 5. (a) Mean cloud boundaries from ship remote sensing observations (gray boxes). Lifting condensation level (LCL) for a parcel with surface humidity and temperature (black lines). Unfilled boxes show mean plus and minus one standard deviation of the mean. (b) Cloud fraction (gray) and LWP (black) with whiskers indicating standard deviation of the mean.

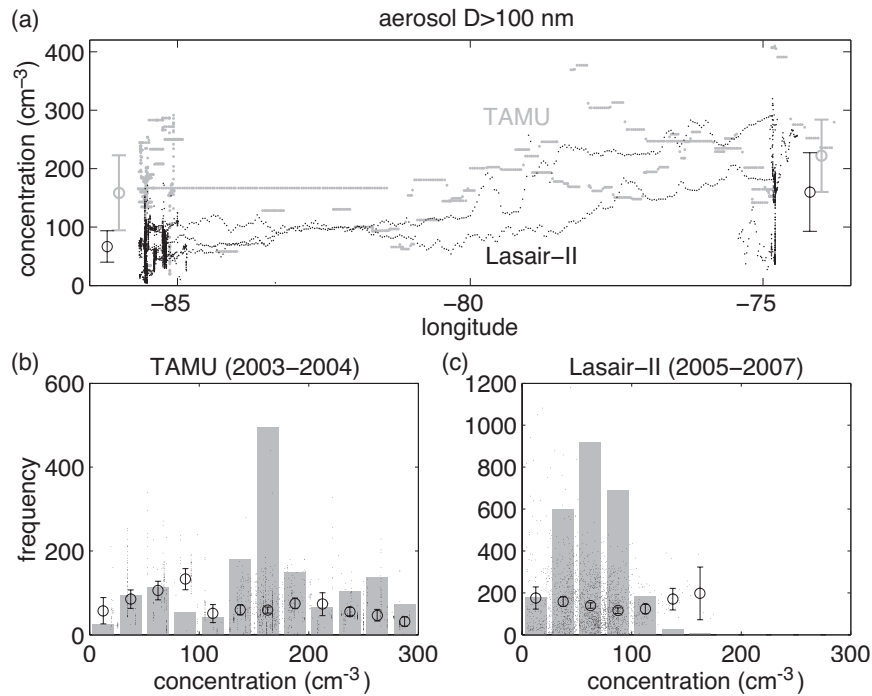


Figure 6. (a) Accumulation mode aerosol concentration (cm^{-3} , $D > 0.1 \times 10^{-6}$ m) along 20°S vs. longitude. Circles and whiskers show mean and standard deviation of the mean west and east of 80°W . (b) Histogram of concentrations in 25 cm^{-3} bins sampled by TAMU in 2003-2004; and (c) histogram for the Lasair-II in 2005-2007. Dots show 10-minute LWP observations; circles and whiskers show LWP mean and standard deviation of the mean for 25 cm^{-3} bins.

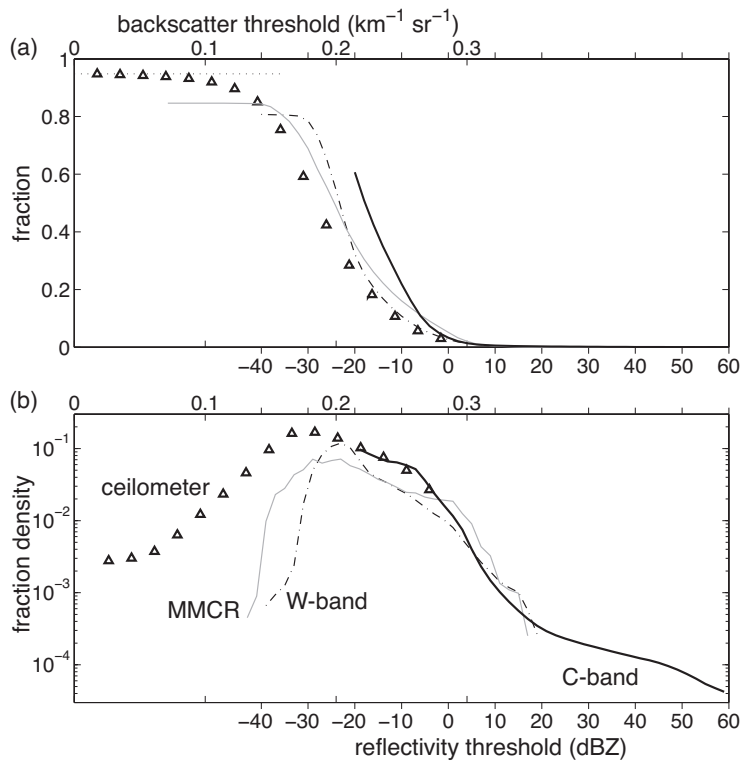


Figure 7. (a) Fraction of sky with reflectivity above a threshold, excluding noise. (b) Probability density as the fraction of full sky per bin (width 2 dBZ or $0.0175 \text{ km}^{-1} \text{ sr}^{-1}$) on a logarithmic scale. Vertically pointing instruments such as the W-band cloud radar (dot-dashed), millimeter cloud radar (MMCR, gray), and ceilometer (triangles) are compared to the C-band scanning radar (solid black). The threshold for the ceilometer is in optical backscatter units ($\text{km}^{-1} \text{ sr}^{-1}$, top axis).

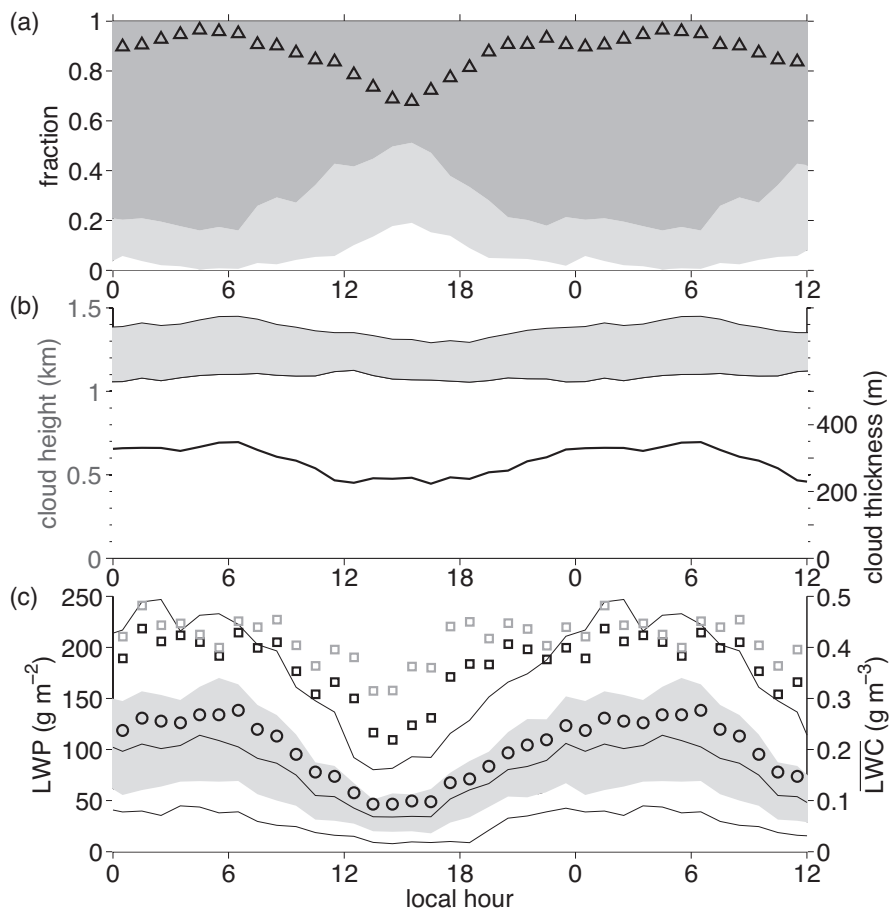


Figure 8. (a) Diurnal cycle of cloud fraction (triangles) for 20°S 75-85°W. Dark gray area corresponds to the fraction of samples with cloud fraction $c=1$, white for $c=0$, light gray for $0 < c < 1$. (b) Diurnal composite mean cloud base and top height (shaded), and cloud thickness (black line). (c) Liquid water path (LWP) mean (circles) and 15, 30, 50, 70, and 85th percentiles. The region 30-70th percentile region is shaded. Squares show vertical average liquid water content (LWC) in the cloud for all sky (black) and cloudy (gray) conditions.

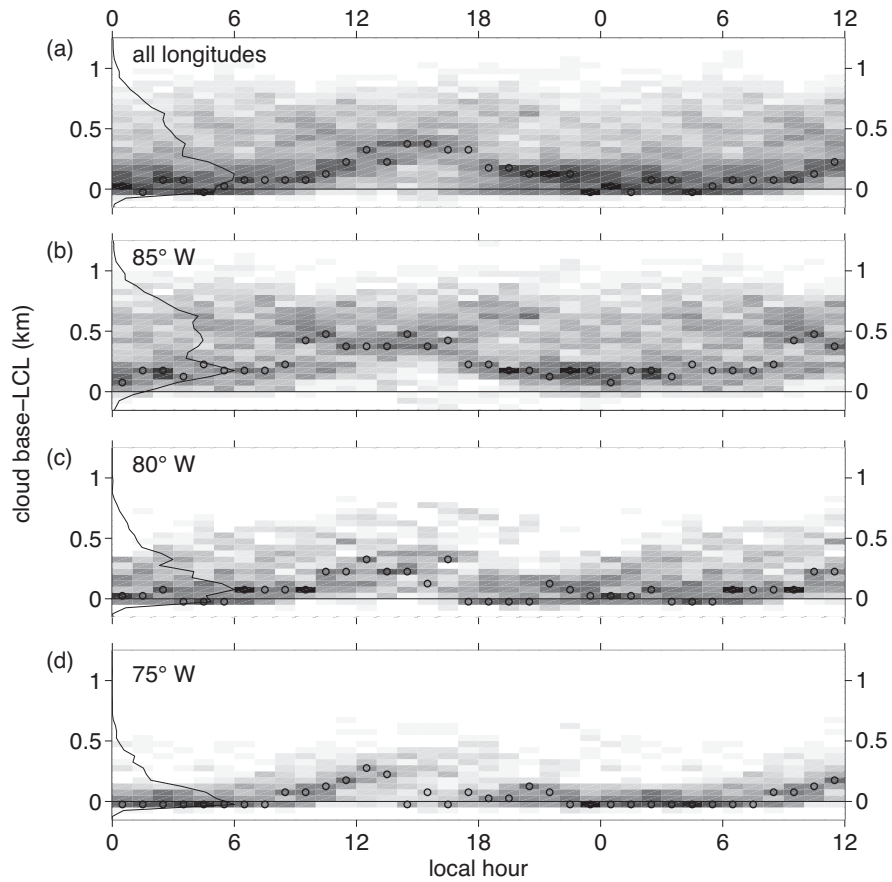


Figure 9. Diurnal cycle of vertical displacement of cloud base height from LCL (CB-LCL) for (a) all longitudes, (b) 85°W, (c) 80°W, and (d) 75°W as in Table 1. Shaded squares show relative frequency in each panel, circles indicate the mode of the distribution. Black lines on the left show normalized probability distributions for all hours. The diurnal cycle is repeated over 1.5 days.

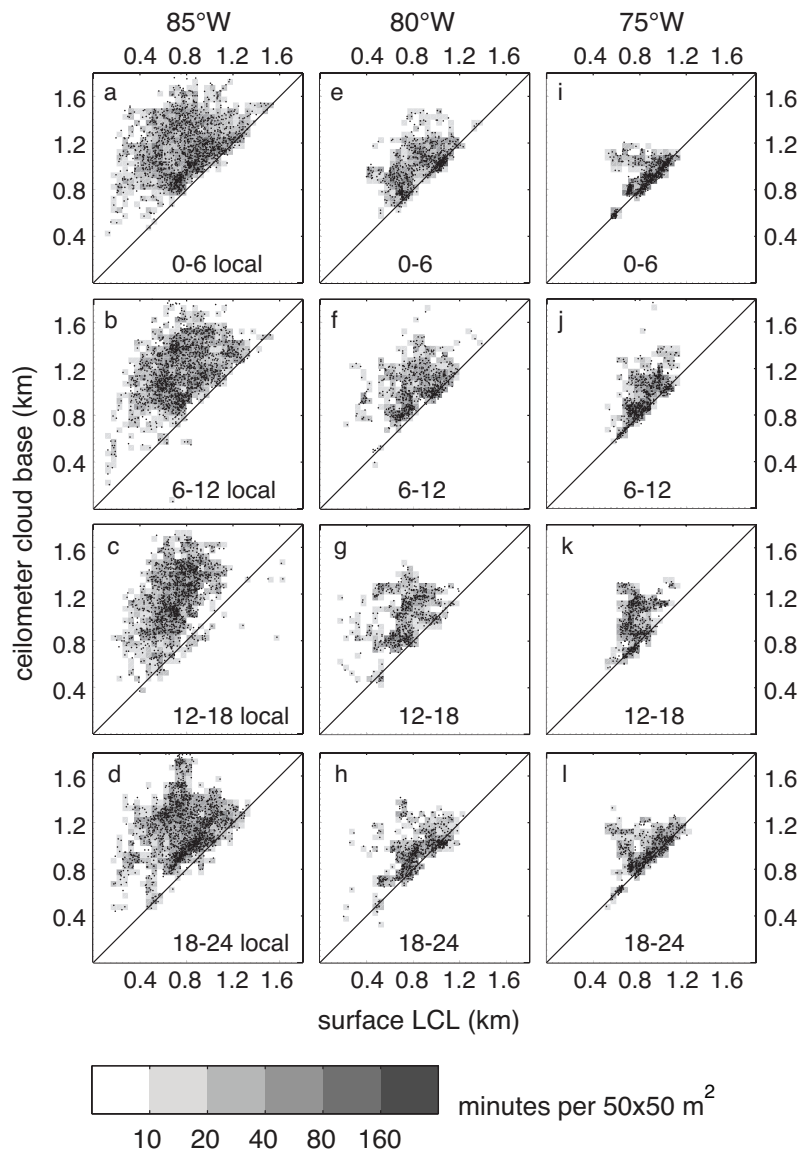


Figure 10. Diurnal cycle scatter plot of cloud base height vs. LCL in four 6-hour increments, 0-6, 6-12, 12-18, and 18-24 hours local (rows); at three longitudes, (a-d) 85°W, (e-h) 80°W, and (i-l) 75°W, 20°S (columns). Black dots indicate coincident 10-minute LCL and cloud base height observations. Shaded squares show joint frequency of LCL and cloud base in 50x50 m² bins.

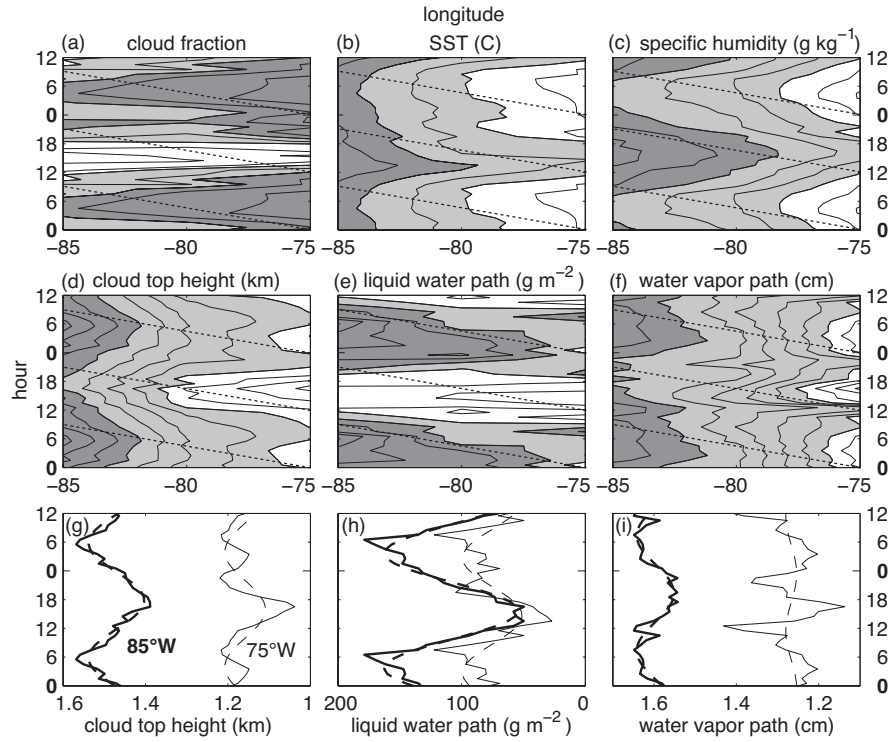


Figure 11. (a-f) Longitude-solar time Hovmöller diagrams of boundary layer and cloud variables along 20°S . Dotted lines show propagation speed for 30 m s^{-1} propagation. Diurnal cycles of (g) cloud top height, (h) liquid water path, and (i) water vapor path at 85°W (bold) and 75°W . Dashed lines show the first diurnal harmonic. The diurnal cycle is repeated over 36 hours.

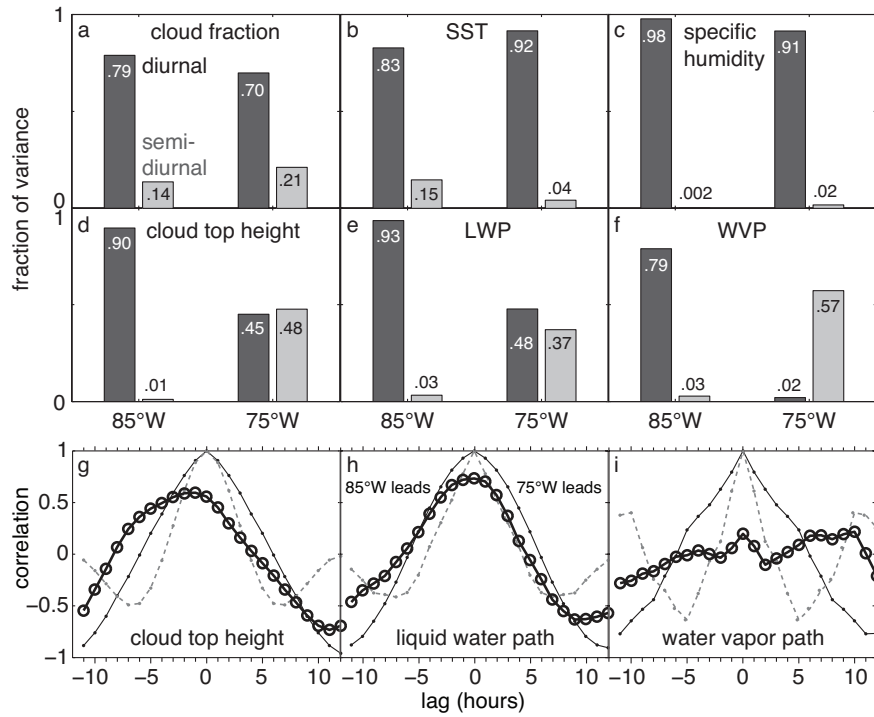


Figure 12. (a-f) Fraction of variance explained by the first diurnal (dark) and semi-diurnal (light gray) components at 85° and 75°W. (g-i) Lag correlation between 75° and 85°W (bold), and autocorrelations at 85°W (solid) and 75°W (dashed). Positive lag indicates 75°W leads 85°W.

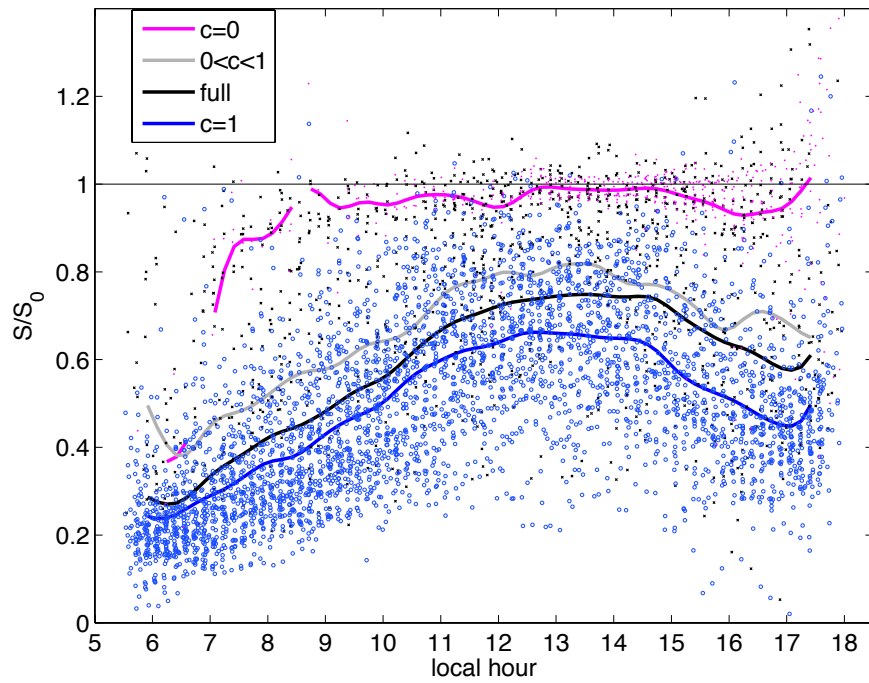


Figure 13. Daylight variation of solar transmission fraction. Magenta dots are for ceilometer cloud fraction of zero, blue dots are for ceilometer cloud fraction of 1. Black crosses show transmission for cloud fraction between 0 and 1. Solid lines show the mean composited on the time of day.

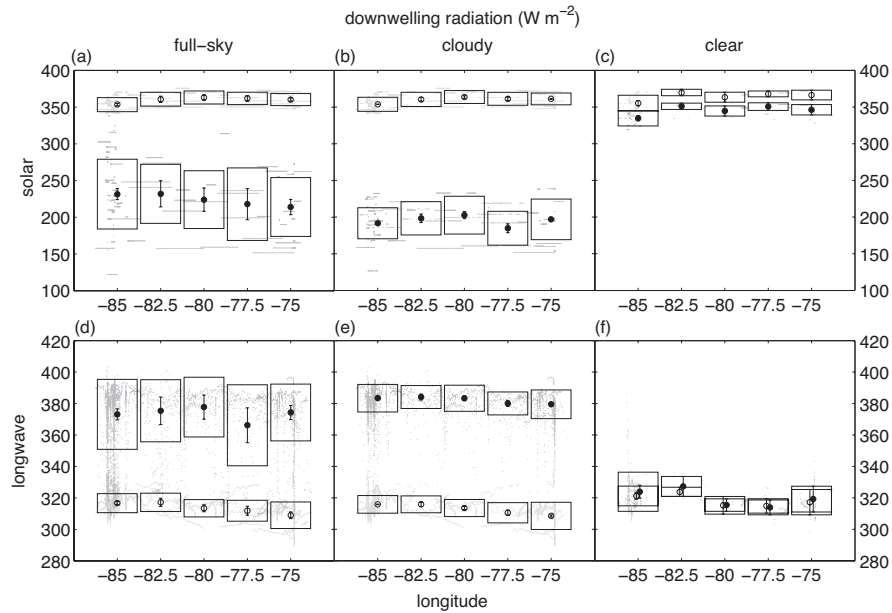


Figure 14. Solar and longwave surface downwelling radiation measured along $20^{\circ}S$ (filled circles) and simulated with a clear-sky model (open circles) in October-November. Full-sky values (a,d); Cloudy conditions (b,e) with ceilometer $c=1$; clear conditions (c,f) $c=0$. Boxes indicate the sampling standard deviation, whiskers the standard deviation of the mean.

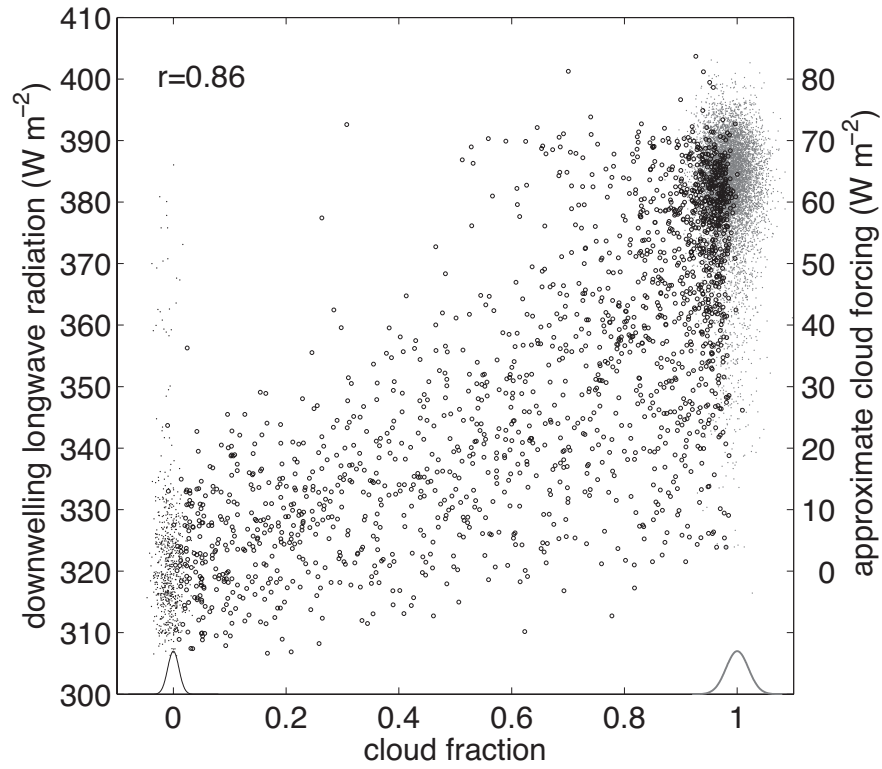


Figure 15. Downwelling longwave radiation vs. cloud fraction for fully clear or cloudy (dots), and partially cloudy skies (circles) in October-November along 20°S. Gaussian random numbers have been added to cloud fractions of 0 or 1 to visualize the distribution.

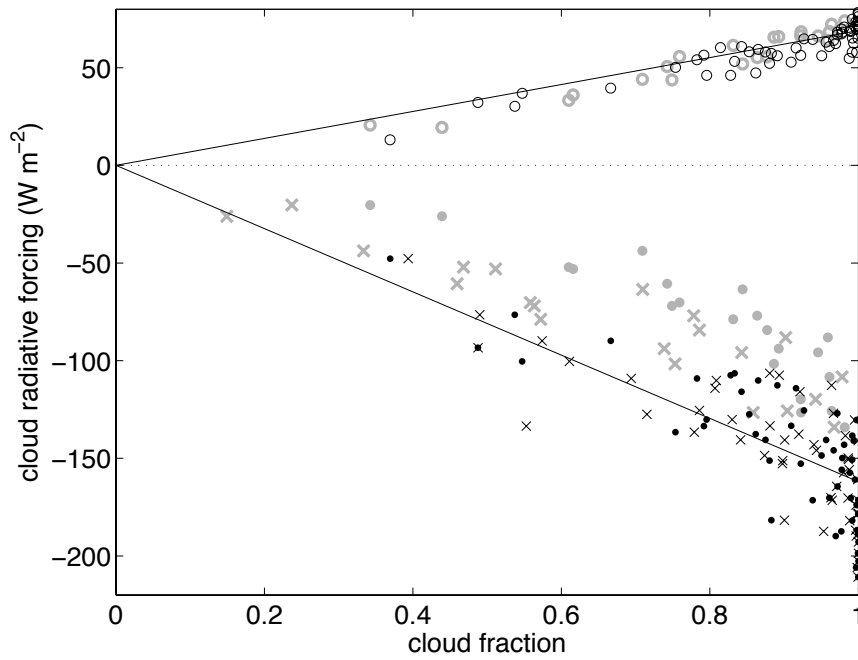


Figure 16. Daily mean cloud radiative forcing as a function of cloud fraction: solar (dots and crosses) and longwave (open circles). Crosses show insolation-weighted cloud fraction for solar cloud radiative forcing. Gray points identify the condition $|S - S_0| < 2(R - R_0) - 10 \text{ W m}^{-2}$.

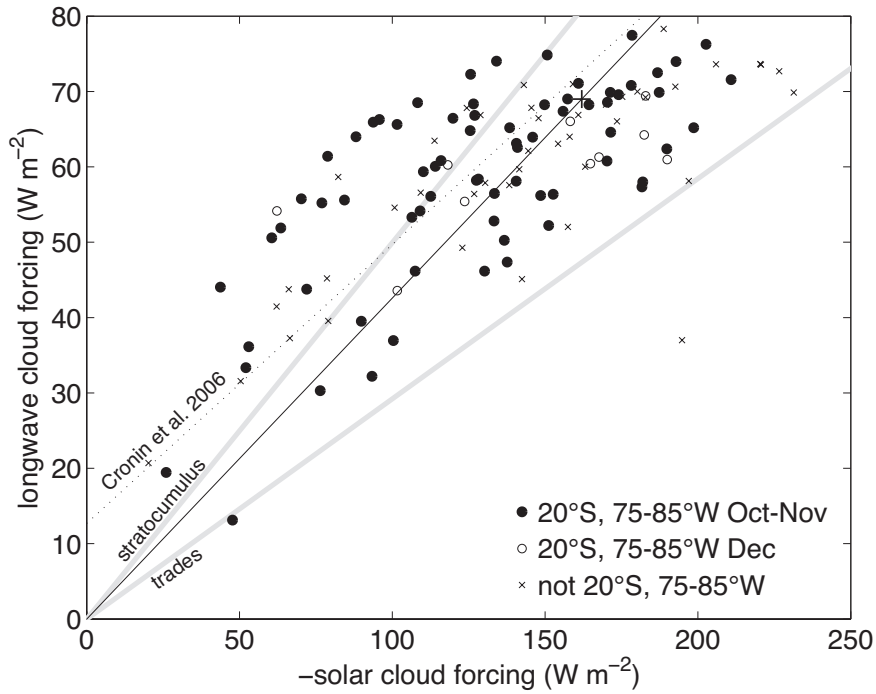


Figure 17. Longwave versus solar cloud forcing phase diagram of daily averages at 20°S, 75-85°W in October-November (filled circles), 20°S December (open circles), and outside the 20°S region (crosses). The black line intersects the maximum cloud forcing (large cross) in Tables 2 and 3. Cloud forcing regressions for stratocumulus and trade cumulus regimes (gray, Fairall et al. 2008), and the regression at the Stratus buoy (dashed, Cronin 2006) are shown.

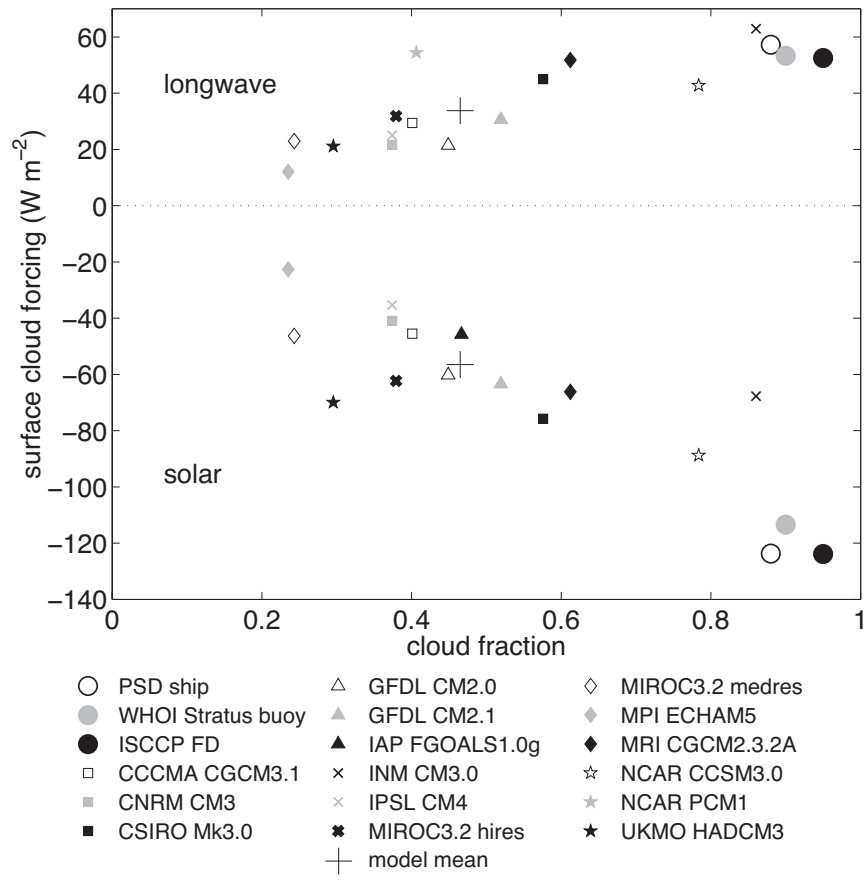


Figure 18. Surface longwave and solar cloud forcing observed (circles) and simulated by coupled GCMs. Cloud fraction for the Stratus buoy and ISCCP FD are provided by MODIS satellite retrievals.

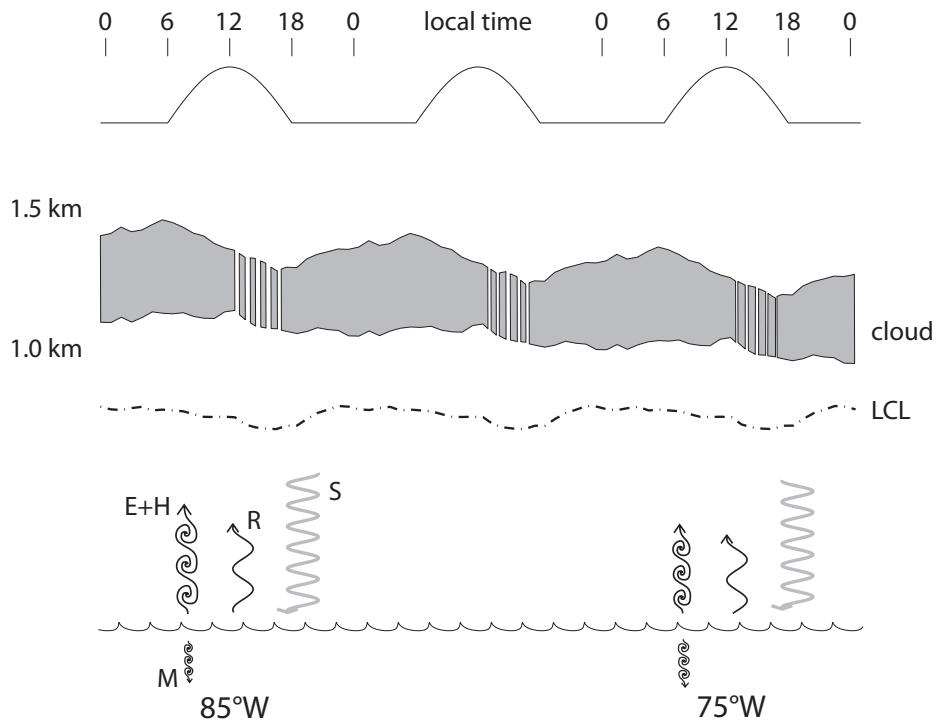


Figure 19. Schematic of the mean longitude structure and diurnal cycle (repeated 3 times) of the marine boundary layer and stratocumulus clouds along 20°S, 85-75°W. Turbulent surface fluxes are presented in de Szoeke et al. (2010).

Tables

Table 1. Idealized 14-level tropical eastern Pacific sounding from 487 rawinsondes along 20°S.

| height (km) | potential temperature (K) | RH (%) | u (m s ⁻¹) | v (m s ⁻¹) |
|----------------|---------------------------------|--------|------------------------|------------------------|
| 0.0 | 290.0 | 70 | -4 | 3.0 |
| 0.1 | 290.0 | 71 | -5 | 4.5 |
| 0.9 | 290.5 | 99 | -5 | 4.5 |
| 1.4 | 291.5 | 99 | -6 | 4.5 |
| 1.5 | 302.0 | 2 | -5 | 2.0 |
| 3.0 | 313.5 | 2 | 0 | 1.0 |
| 5.0 | 322.0 | 2 | 4 | -1.0 |
| 8.0 | 333.0 | 3 | 13 | -4.0 |
| 10.0 | 339.0 | 6 | 19 | -7.7 |
| 13.0 | 348.0 | 12 | 22 | -13.0 |
| 15.8 | 373.0 | 8 | 12 | -7.0 |
| 17.0 | 387.5 | 10 | 7 | -4.0 |
| 17.8 | 405.0 | 12 | 1 | -2.0 |
| 20.0 | 470.0 | 4 | -5 | -0.5 |

Table 2. Total and minimum diurnal (per local hour) sampling for the composite 20°S transect.

| nominal longitude | 85°W | 80°W | 75°W |
|------------------------------|-------------|-------------|-------------|
| longitude range (°W) | 86.25-83.75 | 83-75-76.25 | 76.25-73.25 |
| total hours | 1118 | 456 | 438 |
| minimum hours per local hour | 45 | 17 | 17 |

Table 3. Mean surface clear-sky solar radiation, solar radiation, cloud forcing, and estimates of maximum cloud forcing \pm the standard error of the mean (W m^{-2}). Angle brackets indicate daily averages. Columns show the average for all 7 years of cruises, the average for the 6 years of cruises in October-November, and the average of the cruise in 2004 December. Standard errors of the mean less than the least significant digit (e.g. 1 W m^{-2}) are not listed.

| solar (W m^{-2}) | all cruises | no December | 2004 December |
|---|----------------|----------------|------------------|
| S_0 | 358 \pm 1 | 357 \pm 10 | 366 \pm 2 |
| S | 225 \pm 5 | 226 \pm 5 | 215 \pm 12 |
| $S-S_0$ | -133 \pm 5 | -131 \pm 5 | -150 \pm 12 |
| mean c | 0.86 | 0.88 | 0.74 |
| $(S-S_0)/c$ | -219 \pm 19* | -158 \pm 4** | -488 \pm 77 |
| $\langle S-S_0 \rangle / \langle c \rangle$ | -153 \pm 5 | -146 \pm 5 | -205 \pm 17 |
| \tilde{S}_1-S_0 | -162 \pm 2 | -162 \pm 2 | -167 \pm 2 |

*in all cruises 116 hours of observations (of 1963 hours) were disregarded for having $c=0$, resulting in unbounded $(R-R_0)/c$.

**in Oct-Nov 115 of 1727 hours had $c=0$.

Table 4. Surface longwave clear-sky radiation, longwave radiation, cloud forcing, and estimates of maximum cloud forcing (W m^{-2}) as in Table 2.

| longwave (W m^{-2}) | all cruises | no December | 2004 December |
|---|-------------|----------------|------------------|
| R_0 | 316 | 315 | 329 |
| R | 375 | 373 ± 1 | 391 ± 1 |
| $R - R_0$ | 59 ± 1 | 59 ± 1 | 62 ± 1 |
| $(R - R_0)/c$ | 75 ± 2 | 66 ± 1 | 134 ± 13 |
| $\langle R - R_0 \rangle / \langle c \rangle$ | 68 | 66 | 84 |
| $\tilde{R}_1 - R_0$ | 69 | 69 | 69 ± 1 |

Table 5. Correlations of cloud geometry: cloud top, cloud base (CB), lifting condensation level (LCL), cloud thickness (top-CB), and CB-LCL displacement. Correlations weaker than 0.3 (in parentheses) do not differ from zero with 95% statistical significance, assuming an autocorrelation time scale of 6 hours for 43 degrees of freedom.

| | top | CB | LCL | top-CB | CB-LCL | longitude |
|-----------|--------|-------|---------|---------|---------|-----------|
| top | 1 | 0.73 | 0.45 | (0.26) | 0.37 | -0.37 |
| CB | 0.73 | 1 | 0.52 | -0.48 | 0.60 | -0.46 |
| LCL | 0.45 | 0.52 | 1 | (-0.15) | -0.37 | -0.31 |
| top-CB | (0.26) | -0.48 | (-0.15) | 1 | -0.38 | (0.17) |
| CB-LCL | 0.37 | 0.60 | -0.37 | -0.38 | 1 | -0.20 |
| longitude | -0.37 | -0.46 | -0.31 | (0.17) | (-0.20) | 1 |